The Astrophysical Journal Supplement Series, 247:16 (24pp), 2020 March https://doi.org/10.3847/1538-4365/ab5b98

New Hard-TeV Extreme Blazars Detected with the MAGIC Telescopes*

V. A. Acciari[1], S. Ansoldi[2,3,4], L. A. Antonelli[4], A. Arbet Engels[5], K. Asano[3,4], D. Baack[6], A. Babić[7], B. Banerjee[8], U. Barres de Almeida[9], J. A. Barrio[10], J. Becerra González[1], W. Bednarek[11], L. Bellizzi[12], E. Bernardini[13,14], A. Berti[15], J. Besenrieder[16], W. Bhattacharyya[13], C. Bigongiari[4], A. Biland[5], O. Blanch[17], G. Bonnoli[12], Ž. Bošnjak[7], G. Busetto[14], R. Carosi[18], G. Ceribella[16], M. Cerruti[19], Y. Chai[16], A. Chilingaryan[20], S. Cikota[7], S. M. Colak[17], U. Colin[16], E. Colombo[1], J. L. Contreras[10], J. Cortina[21], S. Covino[4], V. D'Elia[4], P. Da Vela[18], F. Dazzi[4], A. De Angelis[14], B. De Lotto[2], M. Delfino[17,22], J. Delgado[17,22], D. Depaoli[15], F. Di Pierro[15], L. Di Venere[15], E. Do Souto Espiñeira[17], D. Dominis Prester[7], A. Donini[2], D. Dorner[23], M. Doro[14], D. Elsaesser[6], V. Fallah Ramazani[24], A. Fattorini[6], G. Ferrara[4], D. Fidalgo[10], L. Foffano[14], M. V. Fonseca[10], L. Font[25], C. Fruck[16], S. Fukami[3,4], R. J. García López[1], M. Garczarczyk[13], S. Gasparyan[20], M. Gaug[25], N. Giglietto[15], F. Giordano[15], N. Godinović[7], D. Green[16], D. Guberman[17], D. Hadasch[3,4], A. Hahn[16], J. Herrera[1], J. Hoang[10], D. Hrupec[7], M. Hütten[16], T. Inada[3,4], S. Inoue[3,4], K. Ishio[16], Y. Iwamura[3,4], L. Jouvin[17], D. Kerszberg[17], H. Kubo[3,4], J. Kushida[3,4], A. Lamastra[4], D. Lelas[7], F. Leone[4], E. Lindfors[24], S. Lombardi[4], F. Longo[2,26], M. López[10], R. López-Coto[14], A. López-Oramas[1], S. Loporchio[15], B. Machado de Oliveira Fraga[9], C. Maggio[25], P. Majumdar[8], M. Makariev[27], M. Mallamaci[14], G. Maneva[27], M. Manganaro[7], K. Mannheim[23], L. Maraschi[4], M. Mariotti[14], M. Martínez[17], D. Mazin[3,16], S. Mićanović[7], D. Miceli[2], M. Minev[27], J. M. Miranda[12], R. Mirzoyan[16], E. Molina[19], A. Moralejo[17], D. Morcuende[10], V. Moreno[25], E. Moretti[17], P. Munar-Adrover[25], V. Neustroev[24], C. Nigro[13], K. Nilsson[24], D. Ninci[17], K. Nishijima[3,4], K. Noda[3,4], L. Nogués[17], S. Nozaki[3,4], S. Paiano[14], M. Palatiello[2], D. Paneque[16], R. Paoletti[12], J. M. Paredes[19], P. Peñil[10], M. Peresano[2], M. Persic[2,28], P. G. Prada Moroni[18], E. Prandini[4,14], I. Puljak[7], W. Rhode[6], M. Ribó[19], J. Rico[17], C. Righi[4], A. Rugliancich[18], L. Saha[10], N. Sahakyan[20], T. Saito[3,4], S. Sakurai[3], K. Satalecka[13], K. Schmidt[6], T. Schweizer[16], J. Sitarek[11], I. Šnidarić[7], D. Sobczynska[11], A. Somero[1], A. Stamerra[4], D. Strom[16], M. Strzys[16], Y. Suda[16], T. Surić[7], M. Takahashi[3], F. Tavecchio[4], P. Temnikov[27], T. Terzić[7], M. Teshima[3,16], N. Torres-Albà[19], L. Tosti[15], V. Vagelli[15], J. van Scherpenberg[16], G. Vanzo[1], M. Vazquez Acosta[1], C. F. Vigorito[15], V. Vitale[15], I. Vovk[16], M. Will[16], D. Zarić[7], C. Arcaro[4,29], A. Carosi[30], F. D'Ammando[31], F. Tombesi[32,33,34,35], and A. Lohfink[36]

[1] Inst. de Astrofísica de Canarias, E-38200 La Laguna, and Universidad de La Laguna, Dpto. Astrofísica, E-38206 La Laguna, Tenerife, Spain
[2] Università di Udine, and INFN Trieste, I-33100 Udine, Italy
[3] Japanese MAGIC Consortium: ICRR, The University of Tokyo, 277-8582 Chiba, Japan; Department of Physics, Kyoto University, 606-8502 Kyoto, Japan; Tokai University, 259-1292 Kanagawa, Japan; RIKEN, 351-0198 Saitama, Japan
[4] National Institute for Astrophysics (INAF), I-00136 Rome, Italy
[5] ETH Zurich, CH-8093 Zurich, Switzerland
[6] Technische Universität Dortmund, D-44221 Dortmund, Germany
[7] Croatian Consortium: University of Rijeka, Department of Physics, 51000 Rijeka; University of Split—FESB, 21000 Split; University of Zagreb—FER, 10000 Zagreb; University of Osijek, 31000 Osijek; Rudjer Boskovic Institute, 10000 Zagreb, Croatia
[8] Saha Institute of Nuclear Physics, HBNI, 1/AF Bidhannagar, Salt Lake, Sector-1, Kolkata 700064, India
[9] Centro Brasileiro de Pesquisas Físicas (CBPF), 22290-180 URCA, Rio de Janeiro (RJ), Brazil
[10] IPARCOS Institute and EMFTEL Department, Universidad Complutense de Madrid, E-28040 Madrid, Spain
[11] University of Łódź, Department of Astrophysics, PL-90236 Łódź, Poland
[12] Università di Siena and INFN Pisa, I-53100 Siena, Italy
[13] Deutsches Elektronen-Synchrotron (DESY), D-15738 Zeuthen, Germany
[14] Università di Padova and INFN, I-35131 Padova, Italy
[15] Istituto Nazionale Fisica Nucleare (INFN), I-00044 Frascati (Roma), Italy
[16] Max-Planck-Institut für Physik, D-80805 München, Germany
[17] Institut de Física d'Altes Energies (IFAE), The Barcelona Institute of Science and Technology (BIST), E-08193 Bellaterra (Barcelona), Spain
[18] Università di Pisa, and INFN Pisa, I-56126 Pisa, Italy
[19] Universitat de Barcelona, ICCUB, IEEC-UB, E-08028 Barcelona, Spain
[20] The Armenian Consortium: ICRANet-Armenia at NAS RA, A. Alikhanyan National Laboratory, Armenia
[21] Centro de Investigaciones Energéticas, Medioambientales y Tecnológicas, E-28040 Madrid, Spain
[22] Port d'Informació Científica (PIC), E-08193 Bellaterra (Barcelona), Spain
[23] Universität Würzburg, D-97074 Würzburg, Germany
[24] Finnish MAGIC Consortium: Finnish Centre of Astronomy with ESO (FINCA), University of Turku, FI-20014 Turku, Finland; Astronomy Research Unit, University of Oulu, FI-90014 Oulu, Finland
[25] Departament de Física, and CERES-IEEC, Universitat Autònoma de Barcelona, E-08193 Bellaterra, Spain
[26] Dipartimento di Fisica, Università di Trieste, I-34127 Trieste, Italy
[27] Institute for Nuclear Research and Nuclear Energy, Bulgarian Academy of Sciences, BG-1784 Sofia, Bulgaria
[28] INAF-Trieste and Department of Physics & Astronomy, University of Bologna, Italy
[29] Centre for Space Research, North-West University, Potchefstroom 2520, South Africa
[30] Laboratoire d'Annecy de Physique des Particules, Univ. Grenoble Alpes, Univ. Savoie Mont Blanc, CNRS, LAPP, F-74000 Annecy, France
[31] Istituto di RadioAstronomia, Bologna, Italy
[32] Department of Physics, University of Rome "Tor Vergata", Via della Ricerca Scientifica 1, I-00133, Rome, Italy
[33] Department of Astronomy, University of Maryland, College Park, MD 20742, USA
[34] X-ray Astrophysics Laboratory, NASA/Goddard Space Flight Center, Greenbelt, MD 20771, USA

* Contact MAGIC Collaboration (contact.magic@mpp.mpg.de) for queries. Corresponding authors are E. Prandini, C. Arcaro, and V. Fallah Ramazani.

[35] INAF—Astronomical Observatory of Rome, via Frascati 33, 00044, Monte Porzio Catone (Rome), Italy
[36] Department of Physics, Montana State University, P.O. Box 173840, Bozeman, MT 59717-3840, USA
Received 2019 July 30; revised 2019 November 11; accepted 2019 November 11; published 2020 February 20

Abstract

Extreme high-frequency-peaked BL Lac objects (EHBLs) are blazars that exhibit extremely energetic synchrotron emission. They also feature nonthermal gamma-ray emission whose peak lies in the very high-energy (VHE, $E > 100$ GeV) range, and in some sources exceeds 1 TeV: this is the case for hard-TeV EHBLs such as 1ES 0229 +200. With the aim of increasing the EHBL population, 10 targets were observed with the MAGIC telescopes from 2010 to 2017, for a total of 265 hr of good-quality data. The data were complemented by coordinated *Swift* observations. The X-ray data analysis confirms that all but two sources are EHBLs. The sources show only a modest variability and a harder-when-brighter behavior, typical for this class of objects. At VHE gamma-rays, three new sources were detected and a hint of a signal was found for another new source. In each case, the intrinsic spectrum is compatible with the hypothesis of a hard-TeV nature of these EHBLs. The broadband spectral energy distributions (SEDs) of all sources are built and modeled in the framework of a single-zone, purely leptonic model. The VHE gamma-ray-detected sources were also interpreted with a spine–layer model and a proton synchrotron model. The three models provide a good description of the SEDs. However, the resulting parameters differ substantially in the three scenarios, in particular the magnetization parameter. This work presents the first mini catalog of VHE gamma-ray and multiwavelength observations of EHBLs.

Unified Astronomy Thesaurus concepts: Blazars (164); Active galactic nuclei (16); Relativistic jets (1390); BL Lacertae objects (158); X-ray active galactic nuclei (2035); Catalogs (205); Non-thermal radiation sources (1119); Gamma-ray sources (633)

Supporting material: data behind figures, machine-readable table

1. Introduction

Giant elliptical galaxies may host in their center a supermassive black hole ($\sim 10^9\ M_\odot$) which accretes material through a disk and, in 1% up to 15% of the cases (Padovani et al. 2017), features two narrow jets of ultrarelativistic particles extending well outside the galaxy. These objects are known as jetted active galactic nuclei (jetted-AGNs; Urry & Padovani 1995; Padovani 2016). The spectra observed from jetted-AGNs is strongly dependent on the viewing angle of the jet with respect to the observer. This difference is also at the base of their classification. Radio galaxies are jetted-AGNs with the jets seen from large angles. The two extended jets are particularly bright in radio and gamma-rays. On the other hand, blazars are jetted-AGNs seen at small angles, and their spectra are fully dominated by the jet emission, which is largely enhanced due to relativistic effects. They can be subdivided into flat spectrum radio quasars (FSRQs) and BL Lac objects depending on the equivalent widths of emission lines in the optical spectrum (Stickel et al. 1991; Stocke et al. 1991). Ghisellini et al. (2009) suggested that the division between these two classes is due to the different accretion regimes, with FSRQs showing an accretion rate above 10^{-2} of the Eddington rate. The spectral energy distribution (SED) emitted by blazars is characterized by two broad humps (Ghisellini et al. 2017): a low-frequency (from $\sim 10^{12}$ to 10^{18} Hz and above) and a high-frequency peak (above 10^{21} Hz). The first peak is due to synchrotron radiation emitted by ultrarelativistic electrons. The second peak is most likely due to inverse Compton (IC) emission and is possibly accompanied by an additional hadronic component whose relevance is still largely debated (Böttcher et al. 2013). The location of the first peak is on average at quite low frequencies for FSRQs, and drives the division of BL Lac objects into the subcategories LBL, IBL, and HBL (low-, intermediate-, and high-frequency-peaked BL Lac objects, respectively). Fossati et al. (1998) found evidence of an empirical sequence connecting the blazar classes with their bolometric luminosity, that is, low-energy-peaked objects such as FSRQs display a higher luminosity than high-energy-peaked ones, i.e., HBLs, and form the so-called blazar sequence. In addition, the luminosity ratio between the high- and low-energy component increases with bolometric luminosity. According to Ghisellini et al. (1998), this anticorrelation between the peak position of the synchrotron emission and the bolometric luminosity can be explained by effective cooling effects. Effective cooling is more efficient for FSRQs, due to the strong radiation fields within the broad-line region. This leads to a lower Lorentz factor at the break of the electron distribution, which determines the location of both the synchrotron and the Compton peaks, and therefore largely determines the shape of the SED.

The other important parameters characterizing the SEDs of blazars are the ratio of the Compton-to-synchrotron powers, i.e., the Compton dominance, the power injected in the form of electrons, and the power in the external photon component. Because external radiation fields are present in FSRQs, this latter component contributes to effective cooling. Based on blazars with known redshift that have been detected by the Large Area Telescope (LAT) on board the *Fermi Gamma-ray Space Telescope*, Ghisellini et al. (2017) revised the blazar sequence. The authors report to find a sequence with the same general properties as the original one. In addition, when considering BL Lac objects and FSRQs separately, they find that FSRQs form a sequence in Compton dominance and in the X-ray spectral index. However, they do not become redder when being more luminous, while BL Lac objects do.

In this context, Costamante et al. (2001) found evidence of objects with the synchrotron peak frequency exceeding the soft X-ray band, defined as extreme high-frequency-peaked blazars (EHBLs, peak above 10^{17} Hz; see also Abdo et al. 2010a). According to the blazar sequence, these objects are expected to be very faint, being at the upper edge of the peak frequency location. However, several observation campaigns in multibands carried out on blazars have found evidences of a number of relatively bright EHBLs (e.g., 1ES 1426+428;

Costamante et al. 2001) as well as two blazars classified as HBLs that show EHBL behavior during flaring states (e.g., Mrk 501 and 1ES 2234+514; Ghisellini 1999), which are somehow in contradiction with the blazar sequence (e.g., Padovani 2007; Giommi et al. 2011; Kaur et al. 2018).

In the last decade, the very good performances of running Imaging Atmospheric Cherenkov Telescopes (IACTs; namely, H.E.S.S., MAGIC, and VERITAS) opened the possibility of observing this intriguing class of objects at very-high energy (VHE; $E > 100$ GeV). VHE gamma-ray observations are distance limited, due to the interaction of VHE photons with the extragalactic background light (EBL), which causes a suppression of the gamma-ray flux. This suppression increases with the distance of the source and with the energy of VHE photons: for nearby sources ($z < 0.05$), it is effective only above few TeV, but for relatively distant sources ($z > 0.5$), it is already effective at a few hundred GeV. At $z \sim 1.0$, 100 GeV photons are already strongly absorbed (e.g., Franceschini et al. 2008). The current catalog of extragalactic sources detected at VHE by IACTs (TeVCat[37]) counts ~80 objects. The large majority are HBLs with a high-energy (HE) SED peak located typically at or above 100 GeV. Out of these sources, there are 14 sources with published spectra cataloged as EHBLs (Foffano et al. 2019; MAGIC Collaboration et al. 2019a).

There are seven objects detected at TeV energies and classified in Costamante et al. (2018) and MAGIC Collaboration et al. (2019a) as hard-TeV blazars, with a second SED bump peaking above 1 TeV. This translates to a VHE power-law spectral index in the 100 GeV–1 TeV range smaller than 2. The other seven objects are EHBLs with a softer TeV spectra (Foffano et al. 2019). Interestingly, at least other two sources (Mrk 501, Pian et al. 1998, MAGIC Collaboration et al. 2018; 1ES 1959+650, MAGIC Collaboration et al. 2018) have shown EHBL behavior (and hard-TeV spectra) during flaring states. As discussed in Foffano et al. (2019), these different behaviors at VHE gamma-rays might be characterizing different subclasses within the EHBL class. Among TeV-detected EHBLs, 1ES 0229+200 has the highest HE peak frequency.

From the phenomenological and theoretical point of view, the spectral characteristics of hard-TeV EHBLs make these sources extremely interesting objects to be studied in further detail. The prototypical hard-TeV EHBL is 1ES 0229+200, located at a moderate redshift of 0.14 (Aharonian et al. 2007; Tavecchio et al. 2009). The synchrotron peak of 1ES 0229 +200 was sampled in great detail in a multiwavelength campaign carried out in 2010 including optical, UV, and X-ray data which firmly characterized the synchrotron emission of this object (Kaufmann et al. 2011a; Aliu et al. 2014). The high X-ray/UV flux ratios that were observed indicate a remarkably hard synchrotron spectrum, which could hint at the presence of a low-energy cutoff of the electron spectrum (Kaufmann et al. 2011a). Once corrected for EBL absorption, the VHE gamma-ray spectrum indicates a flux that is steadily increasing with energy, suggesting that in this object the HE bump of the SED exceeds few TeV (Aharonian et al. 2007).

Since the detection of its peculiar TeV spectrum, 1ES 0229 +200 has become of fundamental importance for the EBL science case and for constraining the intergalactic magnetic field (IGMF). Due to the extreme hardness of the intrinsic spectrum which does not show any curvature at VHEs up to 10 TeV, 1ES 0229+200 yields the necessary TeV photons to study a wider range of the EBL spectrum up to the, still less constrained, far-infrared band (Aharonian et al. 2007). In the cosmological context, a high intrinsic energy up to 10 TeV is a requisite for deriving limits on the IGMF (Murase et al. 2012). In fact, the photons emitted above 1 TeV from distant EHBLs lead to electromagnetic cascades sensitive to the magnetic field in the intergalactic medium. The IGMF leaves its imprint in the reprocessed gamma-rays, resulting in an excess in the GeV energy range that can be measured with instruments like *Fermi*/LAT (Vovk et al. 2012).

The number of relevant studies carried out on 1ES 0229 +200 justifies and supports the need for deep observations on other objects with similar properties. These studies, in fact, suffer from the very limited sample of hard-TeV EHBLs known both in X-rays and VHE gamma-rays. Considering the extreme properties of their peak components, the investigation of their X-ray and VHE gamma-ray emission is the main goal of the present study. Moreover, it is the first and most important building block to address all of the scientific outcomes briefly introduced above.

It is important to note that in the HE gamma-ray band (100 MeV $< E <$ 100 GeV), faint hard-TeV EHBLs are objects that are very difficult to detect. This is due to a combination of the average low-luminosity characteristics for this kind of objects and the HE peak of the SED located around or above 1 TeV. For example, the *Fermi*-LAT reports a significant detection of 1ES 0229+200 only after 4 yr of exposure time (Vovk et al. 2012; Acero et al. 2015), and despite the hard VHE spectrum, it is not present in the Second Catalog of Hard *Fermi*-LAT Sources, 2FHL (Ackermann et al. 2016).

The paper is structured as follows: in Section 2, a short description of the criteria adopted for the source selection is given followed by a list of the 10 targets of this study. Sections 3–5 report the results of the MAGIC, *Fermi*-LAT, *Swift*-XRT, and *Nuclear Spectroscopic Telescope Array* (*NuSTAR*) data analysis, respectively. Section 5 includes a study of the X-ray temporal properties of the sample. The observational properties of the sources in other bands are briefly outlined in Section 6. The multiwavelength SED data and models are reported and discussed in Section 7. Finally, Section 8 includes a final discussion and a summary of the main results of the paper. The details of the data analyses in the various bands as well as those of the modeling are reported in Appendices A–F.

2. Source Selection

Regarding the selection of EHBL targets for the observation with the MAGIC telescopes, different approaches have been attempted. Such an approach facilitated the chances of detection and takes the updated catalogs into consideration. The general criteria adopted are based on the X-ray spectral behavior, the soft HE gamma-ray spectral behavior, and the X-ray-to-radio flux ratio.

The first criterion (i) relies on the fact that EHBLs are by definition expected to exhibit the synchrotron peak above 10^{17} Hz. Therefore, candidates with a hard spectral index ($\Gamma \leqslant 2$) in the soft X-ray band covered by *Swift*-XRT were targeted. Additionally, the tail of the synchrotron emission could be also detected at hard X-rays by *Swift*/BAT and *NuSTAR*.

The second criterion (ii) adopted for the selection is related to the properties of the HE gamma-ray emission of each source extracted from the following LAT catalogs: the 1FHL, the First

[37] tevcat.uchicago.edu

Table 1
Sample of EHBLs Observed with the MAGIC Telescopes

Source	R.A. (J2000) (°)	Decl. (J2000) (°)	l (°)	b (°)	z	N_H $\times 10^{21}$ (cm^{-2})	$\log(\nu_{peak})$ (Hz)	Selection Criteria
TXS 0210+515	33.57	51.75	135.74	−9.05	0.049[a]	1.440	17.3	i, ii, iv, v
TXS 0637−128	100.03	−12.89	223.21	−8.31	0.136[b]	2.990	17.4	ii, v
BZB J0809+3455	122.41	34.93	186.48	30.35	0.082[c]	0.432	16.6	i, ii, iv, v
RBS 0723	131.80	11.56	215.46	30.89	0.198[c]	0.317	17.8	i, ii, iii, v
1ES 0927+500	142.66	49.84	168.14	45.71	0.187[c]	0.138	17.5	iii, v
RBS 0921	164.03	2.87	249.28	53.28	0.236[c]	0.382	17.9	iii
1ES 1426+428	217.14	42.70	77.48	64.90	0.129[c]	0.113	18.1	i, ii, v
1ES 2037+521	309.85	52.33	89.69	6.55	0.053[a]	4.360	N.A.	i, ii, iv, v
RGB J2042+244	310.53	24.45	67.77	−10.80	0.104[d]	1.010	17.5	ii, v
RGB J2313+147	348.49	14.74	90.5	−41.91	0.163[e]	0.514	17.7	ii, v
1ES 0229+200	38.20	20.29	152.94	−36.61	0.140[a]	0.792	18.5	⋯

Notes. Columns from left to right: source name, equatorial (R.A. and Decl.) and galactic coordinates (l and b), redshift (z), equivalent galactic hydrogen column density reported by Kalberla et al. (2005), synchrotron peak frequency reported by Chang et al. (2017; log ν_{peak}), criteria adopted for the selection (see text for details). 1ES 0229+200, reported in the last line, is the prototype of EHBL sources and is considered in our work as a reference source.
[a] Mao (2011).
[b] S. Paiano (2020, in preparation).
[c] Ahn et al. (2012).
[d] Shaw et al. (2013).
[e] Sowards-Emmerd et al. (2005).

Fermi-LAT Catalog of Sources above 10 GeV (Ackermann et al. 2013), the 2FHL (Ackermann et al. 2016), and the 3FGL, the *Fermi*-LAT 4 yr Point Source Catalog (Acero et al. 2015). The second peak of the SED of EHBLs might be difficult to measure below a hundred GeV, especially when it is located above 1 TeV. This is, for example, the case for 1ES 0229+200, whose second SED peak was constrained above 10 TeV by H.E.S.S. and VERITAS observations. On the other hand, a possible detection, even if marginal, of gamma-rays in the HE gamma-ray range enhances significantly the chance of detectability with MAGIC and makes the extrapolation to the VHE possible. For this reason, the gamma-ray emission properties as reported in the LAT catalogs, when available, have been considered for the selection of new candidates.

In recent MAGIC observation campaigns, the list of EHBL candidates proposed in Bonnoli et al. (2015), where the authors propose new candidates according to the high X-ray-to-radio flux ratio, was considered. This was the third selection criterion (iii).

Fallah Ramazani et al. (2017) proposed a list of 53 promising TeV BL Lac candidates based on the multiwavelength luminosity correlations derived for the sample of TeV-detected BL Lac objects. As the fourth criterion (iv), we selected the best candidates whose X-rays and HE gamma-ray properties follow criteria (i) and (ii).

Finally, low-redshift (<0.2) sources were favored in the selection as criterion (v), ensuring a relatively small effect on the VHE spectra due to EBL absorption, at least below the TeV range.

Sources whose MAGIC spectrum is already published, e.g., 1ES 1741+196 and the recently detected 2WHSP J073326.7+515354 (MAGIC Collaboration et al. 2017a, 2019a), or was collected after 2017 have been excluded from the sample.

The final list of objects observed with the MAGIC telescopes is summarized in Table 1. The equatorial and Galactic coordinates of the sources are listed together with the redshift, equivalent Galactic hydrogen column density reported by Kalberla et al. (2005), and the synchrotron peak frequency as reported in the 2WHSP (Second Wise HSP catalog; Chang et al. 2017), when available. The last column summarizes the criteria used for the selection.

The sample includes the archetypal EHBL source 1ES 0229+200, which has been deeply observed by MAGIC between 2013 and 2017 and is added as a reference source (MAGIC Collaboration et al. 2019b; MAGIC Collaboration 2019, in preparation). All of the considered sources have not been detected by IACTs except for 1ES 1426+428, which was first discovered as a TeV emitter by HEGRA (Aharonian et al. 2002) and recently detected with the VERITAS telescopes (Archambault et al. 2017).

All selected sources show a hard spectral index in the X-ray band and, except for RBS 0921, are listed in the 3FGL catalog. Moreover, all sources selected are present in the 2WHSP of high-synchrotron-peaked blazars except for 1ES 2037+521, whose very bright host galaxy is probably the cause of exclusion from the 2WHSP selection.

3. MAGIC Results

Ten targets were observed with the MAGIC telescopes starting from 2010. A total of 265 hr of good-quality data were collected and analyzed. Table 2 summarizes the general information of MAGIC observations. A fraction of the data was collected during moderate moon time, which explains the relatively high energy threshold reported. The details of the analysis of data taken with the MAGIC telescopes are reported in Appendix A.

For comparison, the results of the analysis of 117.46 hr of 1ES 0229+200 data collected with the MAGIC telescopes between 2013 and 2017 (MAGIC Collaboration 2019, in preparation) are also reported. The significance of the signal from this source is 9σ: although the second SED peak lies in the TeV range, its overall luminosity is low, as predicted by the blazar sequence, and therefore it does not reach a very high significance despite the long exposures.

Table 2
Results of the Signal Search and Integral Flux Analysis of the MAGIC Data for the 10 EHBLs Considered in this Study

Source	Observation Periods	Time (hr)	Significance (σ)	E_{th} (GeV)	Flux$_{\geqslant E_{th}}$ $\times 10^{-12}$(cm^{-2} s^{-1})	L$_{\geqslant 200GeV}$ $\times 10^{43}$(erg s^{-1})	VHE?
TXS 0210+515	2015, 2016, 2017	28.6	5.9	200	1.6 ± 0.5	0.6 ± 0.2	Y
TXS 0637–128	2017	16.4	1.7	300	<8.9[a]	<50.9	N
BZB J0809+3455	2015	21.8	0.4	150	<3.7[a]	<3.0	N
RBS 0723	2013, 2014	45.3	5.4	200	2.6 ± 0.5	24.8 ± 4.8	Y
1ES 0927+500	2012, 2013	26.2	1.2	150	<5.1[a]	<24.2	N
RBS 0921	2016	13.9	−0.4	150	<8.6[a]	<68.5	N
1ES 1426+428	2010	6.5	2.1	200	<9.3[b]	<27.7	N
	2012	8.7	6.0	200	6.1 ± 1.1	18.4 ± 3.4	Y
	2013	5.9	1.8	200	<5.1[b]	<14.2	N
1ES 2037+521	2016	28.1	7.5	300	1.8 ± 0.4	1.3 ± 0.3	Y
RGB J2042+244	2015	52.5	3.7	200	1.9 ± 0.5	3.4 ± 0.8	H
RGB J2313+147	2015	11.5	−0.9	200	<1.5[a]	<7.0	N
1ES 0229+200	2013–2017	117.5	9.0	200	2.1 ± 0.3	7.6 ± 1.1	Y

Notes. The results for 1ES 0229+200 are also reported for comparison, bottom row. Columns from left to right: source name, year(s) of observation, effective exposure time after quality cuts, significance of the signal in σ, assumed energy threshold for integral flux calculation, flux measured above the energy threshold, VHE gamma-ray luminosity over 200 GeV, and the source detection status at VHE gamma-rays (Y: detected, N: not detected, and H: hint of signal). In case of nondetection (see Section 3 for details), an integral flux upper limit is reported instead, assuming a simple power-law spectrum of spectral index Γ (see Equation (1) and the text for further details).

[a] Flux upper limit is calculated by assuming the observed photon index $\Gamma_{obs} = 2.0$.

[b] Flux upper limit is calculated by assuming the observed photon index $\Gamma_{obs} = 2.6$ derived from 2012 observations.

3.1. Signal Search and Integral Flux Analysis

For the signal search, the θ^2 method explained in Appendix A was adopted. The significance of the gamma-ray signal, estimated with formula [17] of Li & Ma (1983), is reported in the fourth column of Table 2.

The analysis revealed firm VHE gamma-ray detection of three new sources, namely TXS 0210+515, RBS 0723, and 1ES 2037+521, and a hint of signal from RGB J2042+244. In addition, a firm detection of the known TeV emitter 1ES 1426+428 was found in the 2012 data set. A dedicated time-resolved analysis was performed on each source. In particular, a possible daily , monthly, and yearly scale variability was checked, and no hint of variability in the analyzed sample was detected. For 1ES 1426+428, a yearly scale analysis resulted in a significant signal detection only from the 2012 data set (see Appendix A). However, with the data collected, the constant-flux hypothesis cannot be excluded ($\chi^2/\mathrm{dof} = 8.439/2$; dof = degrees of freedom). 1ES 1426+428 is the only source of the sample previously detected by IACTs (Djannati-Ataï et al. 2002; Horan et al. 2002; Petry et al. 2002; Aharonian et al. 2003; de la Calle Pérez et al. 2003; Benbow for the VERITAS Collaboration 2011; Fidelis 2012). A comparison of the integral flux and of the observed spectra can be found in Appendix A.

Archambault et al. (2016) reports VHE gamma-ray flux upper limits obtained with the VERITAS array for four sources in our sample. They are TXS 0210+515, BZB J0809+3455, 1ES 0927+500, and RBS 0921. Among these sources, the VHE gamma-ray flux of TXS 0210+515 measured during the MAGIC campaign is in agreement with the upper limit reported by VERITAS, which lies above the MAGIC measurement. In the other three cases, MAGIC observations led to a better constraint of the VHE gamma-ray flux when comparing the reported upper limits by VERITAS. This reflects the deeper exposures adopted by the MAGIC Collaboration. Regarding the variability, it must be underlined that all sources considered are faint TeV emitters, and a possible moderate variability of the signal could be undetectable due to the instrument's sensitivity limit.

3.2. Spectral Analysis

The observed spectra of the three new sources detected with MAGIC, 1ES 1426+428, and for the hint-of-a-signal source are displayed in E^2dN/dE representation in Figure 1 as open gray markers.

All of the spectra are characterized by only three to five spectral points that are affected by large uncertainties, due to the relatively faint signals. Interestingly, all of the sources except the most distant one, that is, RBS 0723, display data points above 1 TeV, which excludes a severe cutoff below this energy as expected for this class of sources, in particular the hard-TeV ones.

The spectra have been fitted with a simple power law of the form

$$\frac{dN}{dE} = F_0 \cdot \left(\frac{E}{E_{\mathrm{dec}}}\right)^{-\Gamma}, \quad (1)$$

with F_0 and Γ as fit parameters representing the flux at the decorrelation energy[38] E_{dec} and the spectral index, respectively, for the observed (Γ_{obs}) and intrinsic spectrum (Γ_{int}). The fit parameters are listed in Table 3. The observed spectra are quite soft, with a spectral index softer than 2, and in the case of RBS 0723, reaching the value 3.60 ± 0.79, where the error is statistical only.

For the sources without a detection (or a hint of a signal) in VHE gamma-rays, flux upper limits were calculated (see Table 2). Given their low redshifts and assuming that their VHE gamma-ray spectra were similar to that of the prototype EHBL 1ES 0229+200, an observed photon index of 2 was

[38] The decorrelation energy corresponds to the energy at which the correlation between flux normalization and spectral index is minimum. The calculation of this energy is based on formula [3] in Abdo et al. (2010b).

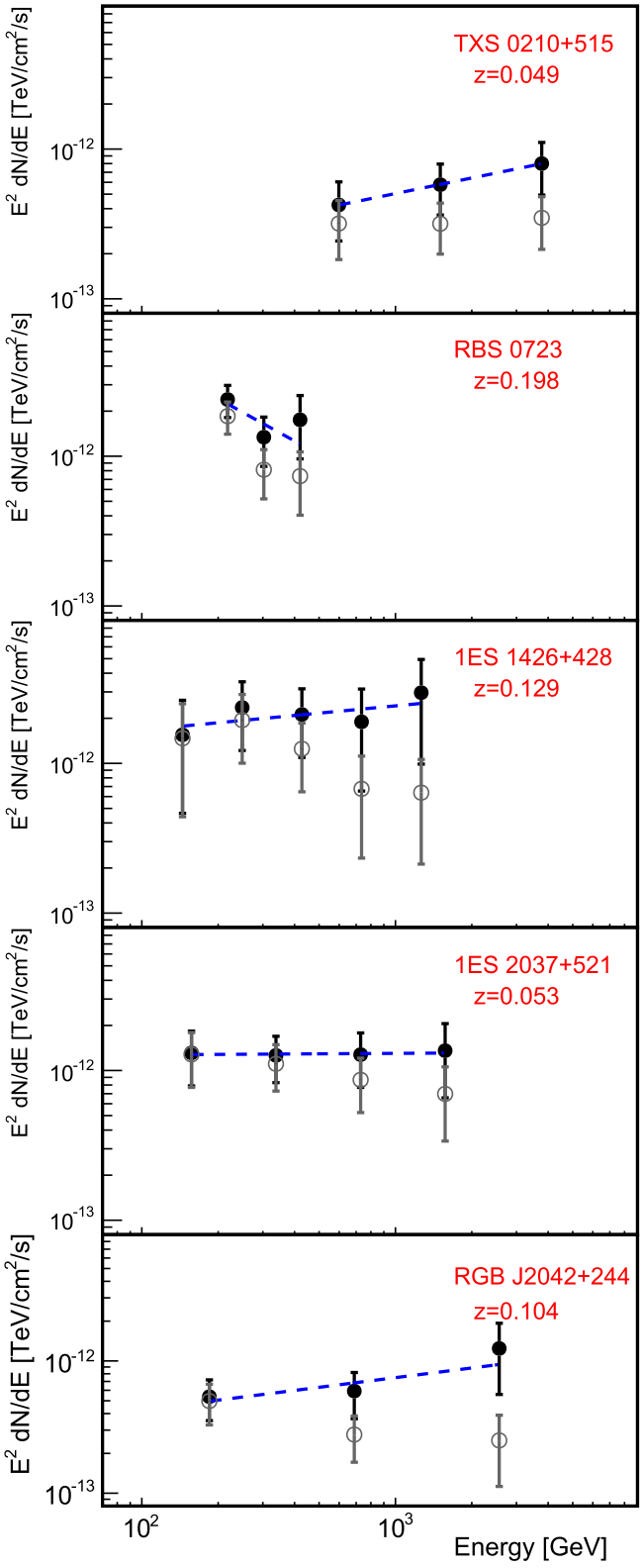

Figure 1. Spectral energy distributions of the four extreme blazars detected with the MAGIC telescopes and for the hint-of-a-signal source in E^2dN/dE representation: observed data (open gray markers) and EBL-corrected data (filled black markers) using the Franceschini et al. (2008) model. The dashed lines represent the power-law fit to the EBL-corrected data.

(The data used to create this figure are available.)

Table 3
Results of the MAGIC Spectral Analysis of the EHBLs Detected at VHE Gamma-Rays Together with the One which Shows a Hint of a Signal (RGB J2042+244) and 1ES 0229+200, the Reference Source

Source	z	E_{dec} (GeV)	$F_0 \times 10^{-12}$ (cm^{-2} s^{-1})	Γ_{obs}	Γ_{int}
TXS 0210+515	0.049	1574	0.10 ± 0.03	2.0 ± 0.3	1.6 ± 0.3
RBS 0723	0.198	300	10.0 ± 2.0	3.6 ± 0.8	2.7 ± 1.2
1ES 1426 +428[a]	0.129	242	25.6 ± 0.1	2.6 ± 0.3	1.8 ± 0.5
1ES 2037+521	0.053	400	5.6 ± 0.6	2.3 ± 0.2	2.0 ± 0.5
RGB J2042 +244[b]	0.104	379	2.6 ± 0.5	2.3 ± 0.3	1.7 ± 0.6
1ES 0229+200	0.140	521	3.6 ± 0.4	2.6 ± 0.1	1.8 ± 0.1

Notes. Columns from left to right: source name, redshift, decorrelation energy, differential energy flux derived from the observed spectrum at the decorrelation energy, spectral index of the observed spectrum, spectral index of the intrinsic spectrum corrected for EBL absorption with the Franceschini et al. (2008) model. Only statistical errors are reported.
[a] Data from 2012 subsample.
[b] Only a hint of a signal was detected for this source.

adopted for the upper limit calculations. For some of the sources, different photon indices (2–4) were assumed to check the robustness of the upper limits. In all cases, the calculated upper limits show small variations when different photon indices are assumed. However, these variations are within the instrument systematic uncertainties (<15%). Given the VHE gamma-ray detection of 1ES 1426+428 in 2012, the observed photon index of 2.6 was used for the calculation of the upper limits for the observation periods in 2010 and 2013, when the source was not detected.

In order to evaluate and compare the intrinsic emission of each source, the observed spectra have been corrected for EBL absorption assuming the model by Franceschini et al. (2008; filled black markers). The indices are reported in Table 3, last column, where the errors listed are statistical only.

MAGIC Collaboration et al. (2019b) tested the effect of using eight different EBL models, including those described by Franceschini et al. (2008) and Domínguez et al. (2011), on the EBL density constraints. Their results show that such an effect is negligible within the tested models.

Very remarkably, the intrinsic spectral indices obtained by fitting with a power-law function (dashed blue lines in Figure 1) are all quite hard, suggesting that the VHE gamma-ray emission covers the energy range still below the second HE SED peak. RBS 0723 represents the only exception, even if the faintness of the signal combined with the large distance severely affects the observed and de-absorbed spectra. Therefore, according to the MAGIC observations TXS 0210+515, whose intrinsic spectral index Γ_{int} is 1.6 ± 0.3, is a newly detected hard-TeV EHBL. 1ES 1426+428 and 1ES 2037+521, $\Gamma_{int} = 1.8 \pm 0.5$ and $\Gamma_{int} = 2.0 \pm 0.5$, respectively, are also compatible with the hard-TeV EHBL nature hypothesis. The hint-of-a-signal source, RGB J2042+244, $\Gamma_{int} = 1.7 \pm 0.6$, seems to also be a hard-TeV EHBL. The extreme position of the second peak in these sources will be further investigated in Section 7.

Table 4
Main Spectral Parameters Resulting from the Analysis of *Swift*-XRT and *Fermi*-LAT Data

Source	*Swift*-XRT				*Fermi*-LAT			
	Obs. date (MJD)	$F_{(2-10\ \mathrm{keV})} \times 10^{-12}$ (erg cm^{-2} s^{-1})	Γ	χ^2/dof	Interval (MJD)	$F_{(1-300\ \mathrm{GeV})} \times 10^{-10}$ (cm^{-2} s^{-1})	Γ	TS[a]
TXS 0210+515	57417	8.6 ± 0.4	1.71 ± 0.04	119.4/77	57388–58118	4.3 ± 1.3	1.8 ± 0.2	42
TXS 0637–128	57784	15.6 ± 1.0	1.96 ± 0.07	32.1/32	54682–58318	3.4 ± 1.1	1.5 ± 0.2	60
BZB J0809+3455	57126	2.1 ± 0.3	1.89 ± 0.08	9.5/17	56658–57753	2.4 ± 0.8	1.9 ± 0.2	39
RBS 0723	56671	13.0 ± 0.7	1.68 ± 0.04	55.3/54	56108–57203	2.8 ± 0.8	1.6 ± 0.2	53
1ES 0927+500	55648	6.4 ± 0.7	2.06 ± 0.07	38.8/26	55562–57022	1.4 ± 0.6	1.5 ± 0.2	30
RBS 0921	57434	4.2 ± 0.6	1.63 ± 0.09	10.7/14		…	…	23
1ES 1426+428	56064	47.4 ± 1.4	1.84 ± 0.02	171.2/172	55927–56292	6.7 ± 1.7	1.4 ± 0.2	94
1ES 2037+521[b]	57660	10.7 ± 1.0	1.93 ± 0.13	18.7/17	57203–57934	4.6 ± 1.5	1.7 ± 0.2	46
RGB J2042+244	57192	9.2 ± 0.8	1.93 ± 0.07	29.5/27	56838–57569	4.6 ± 1.4	1.7 ± 0.2	58
RGB J2313+147	57172	1.6 ± 0.1	2.18 ± 0.06	30.5/32	56838–57569	3.6 ± 1.1	1.7 ± 0.2	34
1ES 0229+200	56264	13.1 ± 1.0	1.79 ± 0.07	43.5/41	56293–58118	2.3 ± 0.7	1.5 ± 0.2	78

Notes. Columns from left to right: source name, *Swift*-XRT observation dates (selected for the SED modeling), X-ray flux in the 2–10 keV energy range, spectral index of X-ray spectrum, fit-statistics parameters, date for *Fermi*-LAT data (centered on the MAGIC observation window), HE gamma-ray flux in the range of 1–300 GeV, spectral index of the HE gamma-ray spectrum, and likelihood test statistics (TS) of the fitted model.
[a] The square root of the TS is approximately equal to the detection significance for a given source.
[b] The X-ray energy range for spectral analysis is 1.5–10 keV (see Appendix C for details).

4. *Fermi*-LAT Results

In general, EHBLs are not strong sources in the HE gamma-ray domain. The shift of the IC peak position to higher energies, together with the average low luminosity of these objects, makes them faint sources for *Fermi*-LAT below 100 GeV.

For the determination of the HE gamma-ray properties of the sources of this study, the analysis of *Fermi*-LAT data was performed. The details of the analysis are reported in Appendix B.

The time span selected for each analysis varies as a function of MAGIC exposure and source faintness. For each source, the interval was selected to be as short as possible to match the MAGIC observations to gather a likelihood test statistic (TS) > 25. Taking into account the low fluxes involved, the minimum interval considered was as long as 1 yr.

In the last four columns of Table 4, the main results of the analyses are reported. For comparison, the 3FGL, 2FHL (Ackermann et al. 2016), and 3FHL (Ajello et al. 2017) values are available in Appendix B.

Only one of the considered sources, namely RBS 0921, is not reported in any *Fermi*-LAT catalog yet. Interestingly, the analysis of more than 8 yr of data from the source RBS 0921 indicates a TS of 23, corresponding to a significance of $\sim 4\sigma$, near the threshold used to define a source detected at HE. The source therefore shows a hint of a signal at HE with this deep exposure and will be possibly detected in the near future. All the other sources are detected with a TS spanning from 34, for the source RGB J2313+147 (1 yr exposure), to 94, for 1ES 1426+428 (1 yr exposure), which is also the brightest source of the sample in X-ray. The fluxes measured in the 1–300 GeV energy range are between 1.4 to 6.7×10^{-10} cm^{-2} s^{-1}. Therefore, in this energy range, the average integral flux of the sources lies within half an order of magnitude. The spectral index values are all below 2, which in the E^2dN/dE representation corresponds to an increasing spectrum. This is consistent with the extreme location of the second SED peak.

The *Fermi*-LAT spectral indices reported in Table 4 are all compatible with the indices measured at higher energies with MAGIC, Table 3. The similar indices are in agreement with the behavior observed in 1ES 0229+200, where the spectrum shows no break from the GeV up to the VHE range above 100 GeV. However, in our case, this compatibility could be simply due to the large error bars affecting the MAGIC determination (in particular for RBS 0723 and TXS 0210 +515). Further, deep VHE measurements are needed to constrain the spectral shape of these EHBLs and determine with precision the location of the HE SED peak.

A study of the relation between the HE spectral properties and the TeV detectability, reported in Appendix B, reveals that there is no evident correlation between the measured LAT spectral index and the TeV detection.

5. X-Ray Properties of the Sample

EHBLs are, by definition, characterized by a synchrotron peak energy exceeding 10^{17} Hz. This means that the bulk of the synchrotron emission is located in the X-ray band. For this reason, special attention has been paid to the X-ray data for the study of the characteristic emission from the selected targets, in particular to those collected with the X-ray Telescope (XRT; Burrows et al. 2004) on board the *Neil Gehrels Swift Observatory* and with the Nuclear Spectroscopic Telescope Array (*NuSTAR*).

5.1. Swift-*XRT Results*

When possible, *Swift*-XRT data simultaneous with MAGIC pointings were requested via Target of Opportunity (ToO) observations. Moreover, all of the available *Swift*-XRT archival data (Stroh & Falcone 2013) have been analyzed using the procedure detailed in Appendix C.

The X-ray light curves of the targets in the 2–10 keV energy range are shown in the left panels of Figure 2. An example of the results is shown in Appendix C. For all the sources, the spectral index Γ of the power law fitting the spectrum is almost $\lesssim 2$. This indicates that the synchrotron peak lies around or

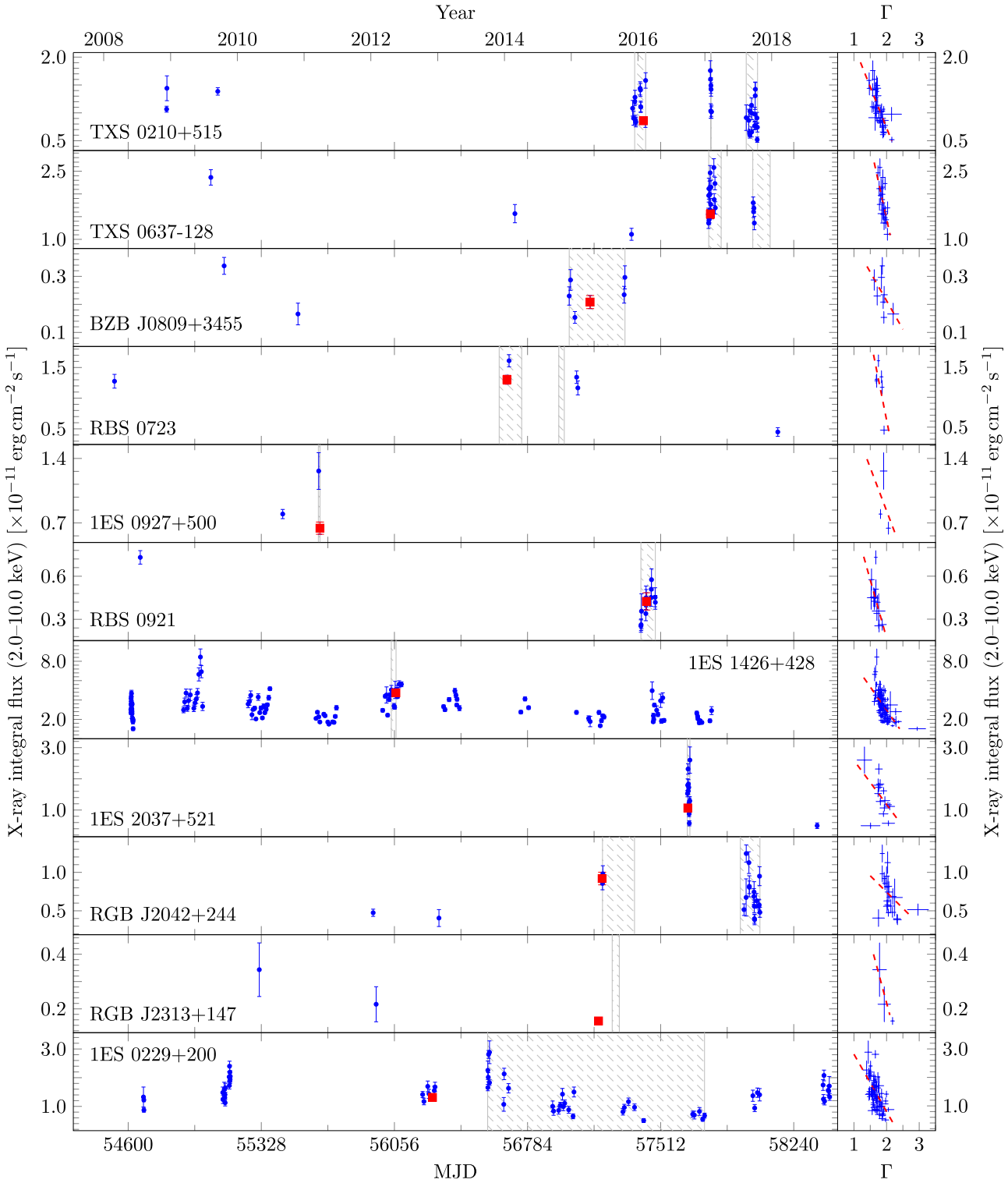

Figure 2. Left panels: X-ray light curve (2–10 keV), corrected for Galactic extinction of the sample. The red squares show the data points which are used in broadband SED modeling. Shaded areas illustrate MAGIC observation windows. Right panels: scatter plot of the power-law photon index (Γ) vs. X-ray flux (2–10 keV) measured with *Swift*-XRT for each source of the sample. Dashed lines are the linear models fitted to the data of each source.

above this energy range, as expected for this class of sources. The only exception is RGB J2313+147, whose X-ray data suggest a peak located below 10^{17} Hz (see Section 5.2).

For broadband SED modeling of each object, we selected the *Swift*-XRT observation, which is either simultaneous with *NuSTAR* observations (TXS 0210+515, RGB J2313+147, and 1ES 0229+200) or has the lowest time lag from the strongest detected signal in the VHE gamma-ray band (Table 4).

As shown in the right panels of Figure 2, the possible relation between Γ and the flux in the 2–10 keV energy band is investigated for each source. The general trend is a harder-when-brighter behavior, meaning that the photon index

decreases when the flux increases. This trend is quite typical in blazars and has been observed in several X-ray campaigns of Mrk 501 (Pian et al. 1998). Mrk 501 is one of the best-sampled BL Lac objects, and it showed an EHBL behavior during some observational campaigns (MAGIC Collaboration et al. 2018). The observed trend can be interpreted as the emerging of an additional population of accelerated electrons in the jet during high-activity states.

It is important to note, however, that there are also counterexamples to this trend, such as the observation campaign on Mrk 501 in 2012, when the source exhibited very hard spectra in the X-ray and VHE ranges both in a quiescent and a flaring state (MAGIC Collaboration et al. 2018). This underlines the overall complexity of blazars when studied in detail.

5.2. NuSTAR *Results*

NuSTAR (Harrison et al. 2013) observed TXS 0210+515 and RGB J2313+147 in the hard X-ray band (3–79 keV) with its two coaligned X-ray telescopes with corresponding focal planes, focal plane module A (FPMA) and B (FPMB), on 2016 January 30 and 2015 May 30, for a net exposure time of 21.4 ks and 22.9 ks, respectively.

NuSTAR data of TXS 0210+515 and RGB J2313+147 have been processed as reported in Appendix D. Simultaneously with *NuSTAR* observations, *Swift*-XRT observations of TXS 0210+515 and RGB J2313+147 were performed. This allows us to study the X-ray spectra of each source over a wide energy range. The results of the simultaneous fits of the *NuSTAR* and *Swift*-XRT data are presented in Table 9 in Appendix D. All errors are given at the 90% confidence level. The photoelectric absorption model `tbabs`, with a neutral hydrogen column density fixed to its Galactic value, was included in all fits. To account for the cross-calibration between *NuSTAR*-FPMA, *NuSTAR*-FPMB, and *Swift*-XRT, a constant factor was included in the model, frozen at 1 for the FPMA spectra and free to vary for the FPMB and XRT spectra. The difference in the cross-calibration for the FPMB spectra with respect to the FPMA spectra is 1%–3%, while for the XRT spectra it is $\leqslant$10% and $\leqslant$15% in the case of TXS 0210+515 and RGB 2313+147, respectively. Madsen et al. (2017) claimed that the relative quality of the spectra plays significant role in the calculation of the cross-normalization constant between the two instruments. The difference in the cross-calibration for the XRT spectra with respect to FPMA is in agreement with their finding.

Two different models were tested: a simple power-law and a log-parabola model. For TXS 0210+515, the F-test shows an improvement of the fit with a log-parabola model with respect to a simple power law, with a probability of 9.8×10^{-9} that the null hypothesis is true. The log-parabola model is therefore preferred with a 5.7σ level of confidence. The combined *Swift*-XRT and *NuSTAR* spectrum of TXS 0210+515 is reported in Appendix D.

In the case of RGB 2313+147, the X-ray spectrum is well fitted by a simple power law (Figure 9 in Appendix D). However, the X-ray flux observed during the *NuSTAR* observation of RGB 2313+147 is a factor of 10 lower with respect to the value observed for TXS 0210+515. In this way, the relatively low number of counts may prevent us from accurately testing a curved spectrum in X-rays.

1ES 0229+200 was also observed with *NuSTAR* on 2013 October 2, 6, and 10, for a total exposure time of ~51 ks. We adopt here the data analysis results published in Costamante et al. (2018). Also, in this case, a log-parabola model is statistically preferred over a simple power-law model.

6. Properties of the Sample in Other Bands

All 10 targets considered in the study have radio data accessible via public archives that were recovered from the NED database.[39] The apparent radio flux values measured at 1.4 GHz are distributed from 4 to 500 mJy. The corresponding absolute powers are distributed in the range (1–6) $\times 10^{33}$ W.

The XRT data presented in the previous section have always been complemented with data at lower frequencies collected with the UVOT instrument, on board the *Swift* satellite. Apart from the bands at larger energies, in the UV domain (when available), the UVOT data generally represent the emission from the host galaxy. In extreme blazars, in fact, the host galaxy is clearly detected at IR–optical wavelengths, as the synchrotron peak is shifted toward the X-ray regime. This is not the usual case for other kinds of BL Lac objects, where the host galaxy is usually dominated by the peak of the nonthermal continuum.

Five sources of the sample are reported in the *Swift*-BAT 105 Month Hard X-ray catalog[40]; they are TXS 2010+515, TXS 0637–128, 1ES 0927+500, 1ES 1426+428, and 1ES 0229+200 (Oh et al. 2018). Interestingly, three of those sources have been detected by MAGIC, suggesting that the detection in hard X-rays is a good (but not exclusive) selection criterion for VHE observations.

7. SED Modeling

The SEDs of each target are assembled complementing the MAGIC, *Swift*-XRT, *NuSTAR*, and *Fermi*-LAT data with archival data from the ASI Space Science Data Center (SSDC).[41] VHE gamma-ray data are corrected for the EBL absorption effect by adopting the Franceschini et al. (2008) model, which is in good agreement with current limits for the diffuse background (Cooray 2016).

The SEDs are displayed in Figure 3. The archival data are shown in gray while the data used for the modeling are displayed with red open markers and red downward triangles in the case of upper limits. These data can be considered to be quasi-simultaneous, with MAGIC and *Fermi*-LAT data being integrated over a long period, due to the relatively faint emission, and *Swift*-XRT and *NuSTAR* spectra taken from one observation within the MAGIC observation window. For 1ES 0229+200, the *NuSTAR* data recently published in Costamante et al. (2018) were adopted. In the case of 1ES 1426+428, the average 14–195 keV spectrum obtained with *Swift*-BAT in 105 months of survey from 2004 to 2013 (Oh et al. 2018) was included in the archival (gray) SED and clearly constrains the peak position in the extreme region, above 10^{17} Hz.

7.1. Synchrotron Self-Compton Model

To fit the broadband spectra, first, the numerical code in Asano et al. (2014) (see also Asano & Hayashida 2015, 2018), which calculates the emission from a conical jet, is adopted. In

[39] https://ned.ipac.caltech.edu
[40] https://swift.gsfc.nasa.gov/results/bs105mon/
[41] http://www.asdc.asi.it

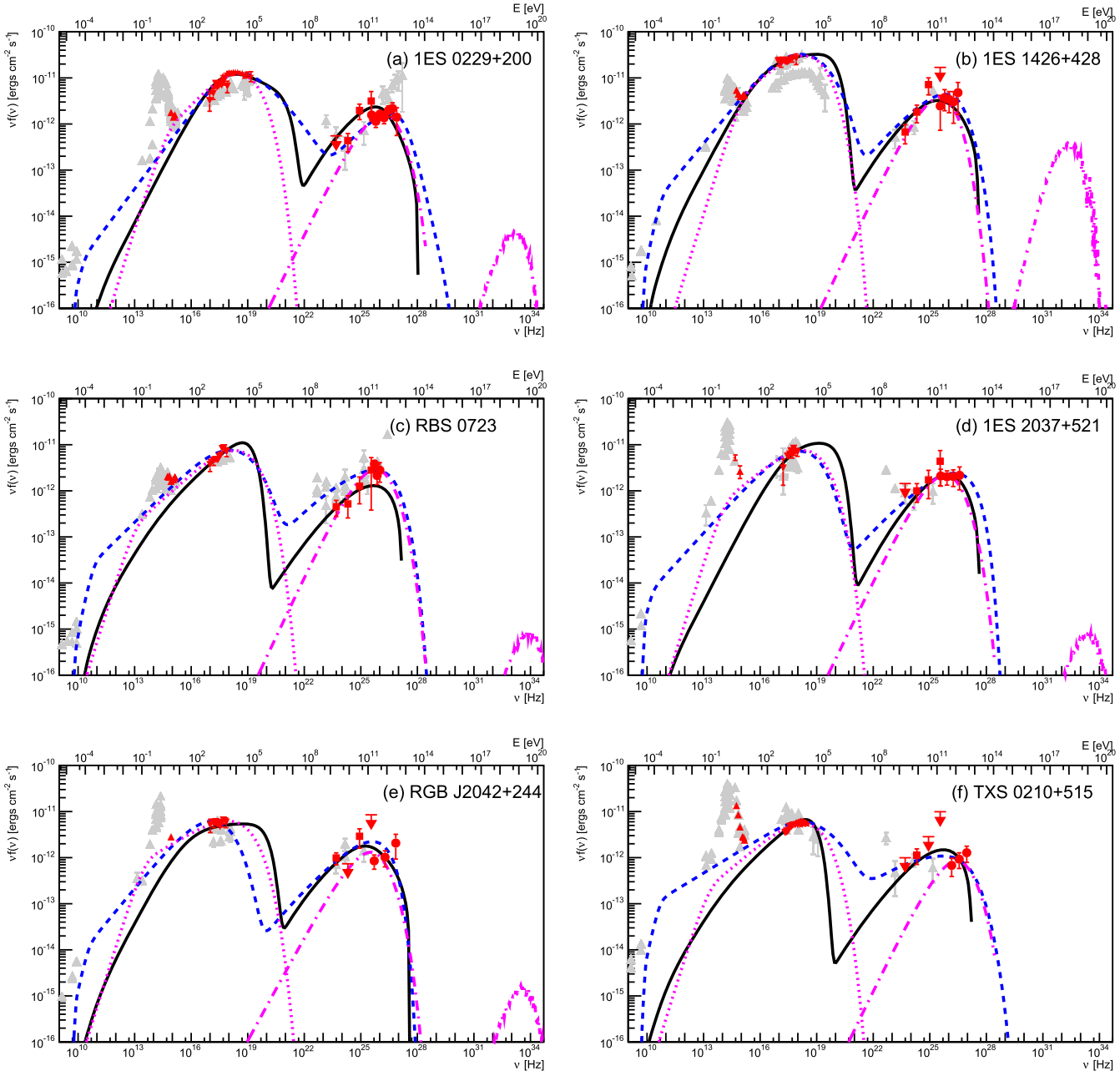

Figure 3. Broadband SED and modeled spectrum for 1ES 0229+200 (archetypal EHBL) and the four VHE gamma-ray sources detected with MAGIC presented in the study. The broadband SED of RGB J2042+244, for which a hint of a signal was detected at VHE gamma-rays, is also shown. Red points represent contemporaneous UVOT, XRT, *NuSTAR*, *Fermi*-LAT, and MAGIC data considered in the fit. Gray markers are archival data from the ASDC website. The blue dashed line is the result of the conical jet SSC model. The black continuous line represents the outcome of the spine–layer model. The dashed-dotted magenta line is the outcome of the proton synchrotron model. The third bump in the proton synchrotron model is the expected neutrino flux resulting from the best-fit solution proposed. Details in the text.

(The data used to create this figure are available.)

this code, the temporal evolution of the electron and photon energy distributions in the plasma rest frame are calculated along the jet. In the steady outflow scenario, the temporal evolution along the jet is equivalent to the radial evolution, so that the emission in this code is obtained from the integral of the 1D structure. This treatment is similar to the BLAZAR code by Moderski et al. (2003), which has been frequently adopted to reproduce blazar spectra (see, e.g., Kataoka et al. 2008; Hayashida et al. 2012). The conically expanding jet naturally leads to the adiabatic cooling of electrons, which is a similar effect to the electron escape in one-zone steady models. Thus, the electron escape in this 1D code can be ignored.

The injection of the nonthermal electrons starts from an initial radius $R = R_0$. The electron injection is assumed to continue during the dynamical timescale $R_0/(c\,\Gamma)$ in the plasma rest frame. In this timescale, the injection rate into a given volume V, which is expanding as $V \propto R^2$, is assumed to be constant. Even after the shutdown of the electron injection, the electron energy distribution and photon emission are calculated as far as $R = 10\ R_0$. The injection rate is normalized by the

electron luminosity L_e in the observer frame. The electron energy distribution at injection is a single power law with an exponential cutoff, $\dot{N}(\gamma) \propto \gamma^{-p_1} \exp(-\gamma/\gamma_{\rm max})$ for the electron Lorentz factor $\gamma > \gamma_{\rm min}$, or a broken power-law energy distribution, changing the index from p_1 to p_2 at $\gamma = \gamma_{\rm br}$. The magnetic field in the plasma frame evolves as $B = B_0(R_0/R)$ in the code. Synchrotron IC scattering with the Klein–Nishina effect, $\gamma\gamma$-absorption, secondary pair injection, synchrotron self-absorption, and adiabatic cooling are taken into account.

In this paper, the jet-opening angle is assumed to be $1/\Gamma$, where Γ is the bulk Lorentz factor of the jet, and an on-axis observer (the viewing angle is zero) is considered. The photon flux is obtained by integrating over the entire jet, taking into account the Doppler boosting by the conically outflowing emission region.

The data cannot constrain all of the model parameters. Here, the initial radius is fixed at a typical value of $R_0 = 0.03$ pc, and the minimum Lorentz factor at $\gamma_{\rm min} = 20$. The remaining five model parameters, i.e., Γ, B_0, electron luminosity L_e, maximum electron Lorentz factor $\gamma_{\rm max}$, and spectral index p_1 are left free to vary. The broken power-law model includes two additional parameters, that is, the break Lorentz factor $\gamma_{\rm br}$ and the HE spectral index p_2. The parameters in the fits are summarized in Table 10 in Appendix E together with the values obtained from the fits: the synchrotron peak frequency ($\nu_{\rm syn,pk}$), the IC peak frequency ($\nu_{\rm IC,pk}$), the Compton dominance parameter (the ratio of $\nu\, L_\nu$ at $\nu_{\rm syn,pk}$ to that at $\nu_{\rm IC,pk}$, dented as "CD"), and the energy density ratio of the magnetic field with that of the electrons (U_B/U_e) at the radius where the electron injection terminates.

Note that the Klein–Nishina effect is crucial in EHBLs. If we can use the well-known relation $\nu_{\rm IC,pk} \sim \gamma^2_{\rm max}\, \nu_{\rm syn,pk}$ or $\nu_{\rm IC,pk} \sim \gamma^2_{\rm br} \nu_{\rm syn,pk}$ in the Thomson regime, the parameter estimate is straightforward. However, the photon energy in the electron rest frame is much higher than $m_e c^2$ in EHBLs, so that the simple estimate for $\nu_{\rm IC,pk}$ is not useful because of the Klein–Nishina effect. Our numerical code, which includes the Klein–Nishina effect, outputs a consistent magnetization, which is much less than the Compton dominance parameter introduced above.

First, we consider 1ES 0229+200, the prototype of EHBLs. As shown in Figure 3(a), the *NuSTAR* data provide the spectral shape around the synchrotron peak very well. This sharp break cannot be reproduced by the cooling break, so that the broken power-law injection is adopted. The model is in good agreement with the observed quasi-simultaneous data. Assuming the synchrotron radiation is the dominant cooling process, the cooling break in the electron energy distribution is expected to appear at

$$\gamma_{\rm c} = \frac{6\pi m_e c^2 \Gamma}{\sigma_T B^2 R_0}. \tag{2}$$

This corresponds to an observed photon energy

$$\varepsilon_{\rm syn,c} = \frac{3}{2}\Gamma \frac{\hbar e B}{m_e c}\gamma_{\rm c}^2 \tag{3}$$

$$\simeq 8.7 \left(\frac{\Gamma}{20}\right)^3 \left(\frac{B}{0.1\ {\rm G}}\right)^{-3} \left(\frac{R_0}{0.03\ {\rm pc}}\right)^{-2} {\rm keV}. \tag{4}$$

In the modeled spectrum, the break energy at ∼10 keV due to $\gamma_{\rm br}$ and the cooling break at ∼300 keV are consistent with a magnetic field of 0.03 G at the radius where the electron injection terminates. The magnetization parameter $U_{\rm B}/U_e$ is very low ($\sim 10^{-3}$) in this model.

The MAGIC data show a significantly dimmer and softer spectrum than those observed in 2005–2006 by H.E.S.S. (Aharonian et al. 2007). Taking into account the H.E.S.S. data for the one-zone synchrotron self-Compton (SSC) model by Kaufmann et al. (2011b) requires a very narrow electron energy distribution ($\gamma_{\rm min} = 3.9 \times 10^5$, $\gamma_{\rm br} = 6.2 \times 10^7$). While the size of the emission region in their model is only a factor of ∼2 larger than ours, their magnetic field is much lower (3.2×10^{-5} G). Costamante et al. (2018) also fitted the broadband spectrum of this source, adopting the same X-ray data as included in our modeling, but using the H.E.S.S. data. With $U_B/U_e = 5.9 \times 10^{-6}$–$5.0 \times 10^{-5}$, the magnetization parameter in their models is also extremely low. However, with the mild variability shown in VHE gamma-rays of 1ES 0229 +200 (VERITAS; Aliu et al. 2014) and the nonsimultaneity of the *Swift* and H.E.S.S. data, the modeling can be affected. The fitting result with the MAGIC data agrees with a more conservative electron energy distribution and magnetization.

The synchrotron spectral peak for 1ES 1426+428 is not well constrained by the data collected during the MAGIC observing period (see Figure 3(b)). Referring to the historical data, a single power-law injection model with the peak energy $\varepsilon_{\rm syn,pk} \sim 6$ keV is adopted in that figure. In this case, a larger magnetic field is adopted, implying that the synchrotron peak is due to the cooling break. The broad shape of the synchrotron peak leads to a relatively higher photon flux in the lower energy range. When the Klein–Nishina effect becomes crucial, the higher density of low-energy photons enhances the efficiency of SSC emission. The relatively broad spectral peak and different IC peak energies in 1ES 1426+428 lead to a large difference in the magnetization parameter even for a Compton dominance parameter similar to that of 1ES 0229+200.

Compared to the synchrotron spectral shape, the observed gamma-ray spectrum is very hard. Thus, the model has difficulty in reproducing the hard *Fermi* spectrum. Here, we give weight to the MAGIC data points, and the broadband spectrum is fitted.

For RBS 0723 (Figure 3(c)) compared to the synchrotron spectral shape, the observed HE gamma-ray spectrum is very hard. Thus, the model has difficulty reproducing the hard *Fermi*-LAT spectrum. Here, we give weight to the MAGIC data points, and the broadband spectrum is fitted. The single power-law injection model reproduces the synchrotron and SSC flux in the VHE band, while the *Fermi*-LAT flux lies below the model expectations. The synchrotron spectral peak is adjusted by the maximum electron energy. The cooling break is higher than $\varepsilon_{\rm syn,pk}$ in this case. The IC flux of the modeled spectrum is slightly higher than the *Fermi* flux, but consistent with the flux in other observational periods (in gray).

The hard X-ray spectrum in 1ES 2037+521 indicates a peak energy higher than 4 keV. The model shown in Figure 3(d) assumes the synchrotron peak to be determined by the electron maximum energy. Because the synchrotron peak is not constrained, we can increase $\varepsilon_{\rm syn,pk}$ with a larger $\gamma_{\rm max}$, which further leads to a low magnetic field. The magnetization obtained in 1ES 2037+521 is the lowest among our results. Adopting a higher magnetic field, the break appears below 4 keV. Among the models presented in this paper, 1ES 2037 +521 has the highest $\varepsilon_{\rm syn,pk}$, which is close to 100 keV. This is

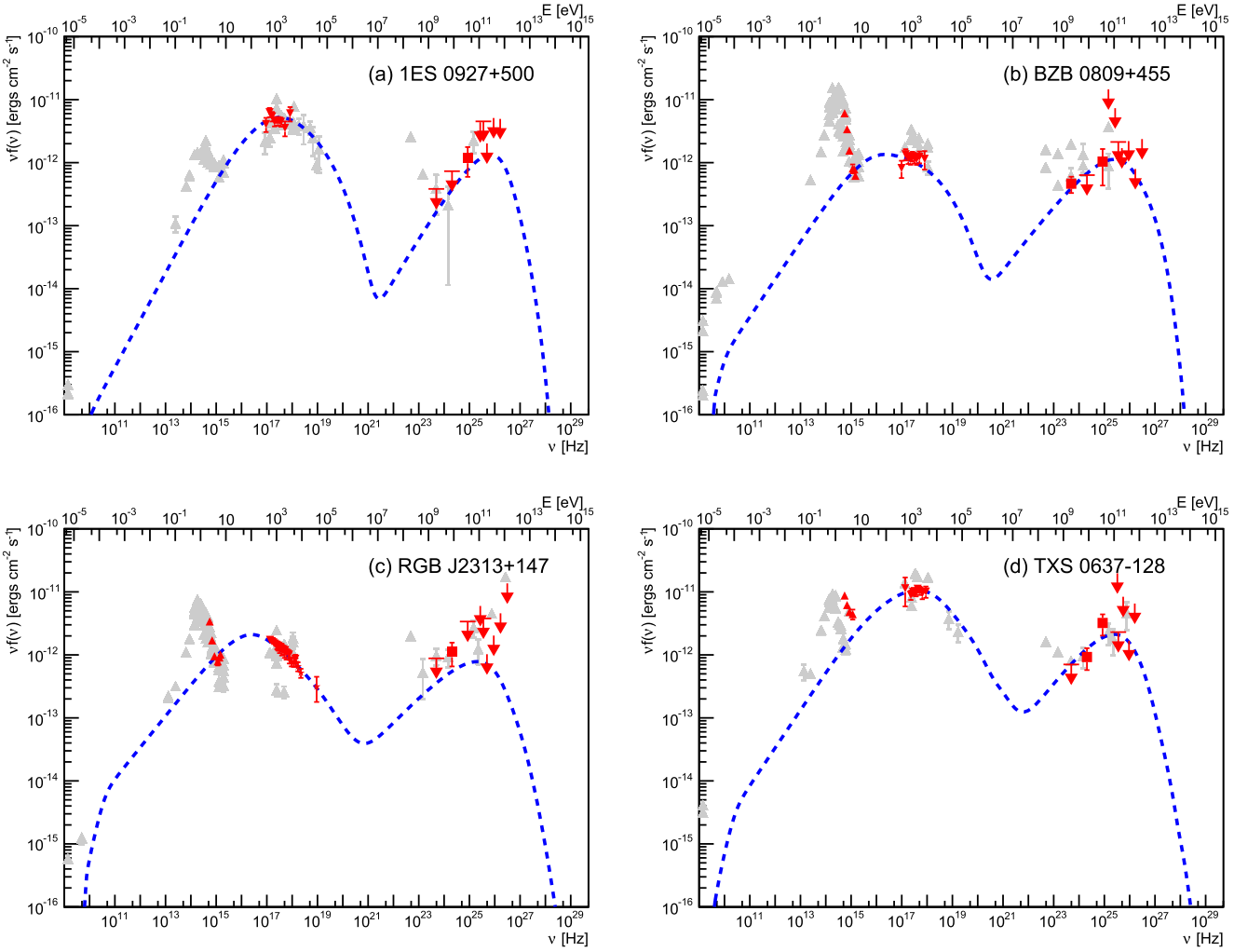

Figure 4. Broadband SED and modeled spectra for four sources with no MAGIC detection or hints (but *Fermi*-LAT detection) presented in the study. Red points represent contemporaneous UVOT, XRT, *NuSTAR*, *Fermi*-LAT, and MAGIC data considered in the fit. Gray markers are archival data from the SSDC website. The blue dashed line is the result of the conical jet SSC model. Details in the text.

(The data used to create this figure are available.)

much higher than the highest value (∼9 keV) confirmed for BL Lac objects in the steady state (Costamante et al. 2018). The flat spectrum obtained with MAGIC seems consistent with the SSC peak of the modeled spectrum.

Assuming that the flat X-ray spectrum in RGB J2042+244 corresponds to the synchrotron peak, the spectrum is fitted adopting a relatively lower value for the maximum energy of electrons as shown in Figure 3(e).

The synchrotron peak in TXS 0210+515 is relatively well constrained. To reconcile the flat gamma-ray spectrum, especially for the *Fermi* data, we need to assume a soft electron energy distribution as $p_1 = 2.5$, which implies that the energy budget is dominated by low-energy electrons. As a result, the magnetization is one of the lowest, at $\sim 10^{-4}$.

There are five sources for which MAGIC provides only upper limits in VHE flux. Even in these cases, the upper limits can constrain the model. In 1ES 0927+500, there are significant upper limits at roughly 600 MeV and 200 GeV by *Fermi* and MAGIC, respectively, while the source was detected

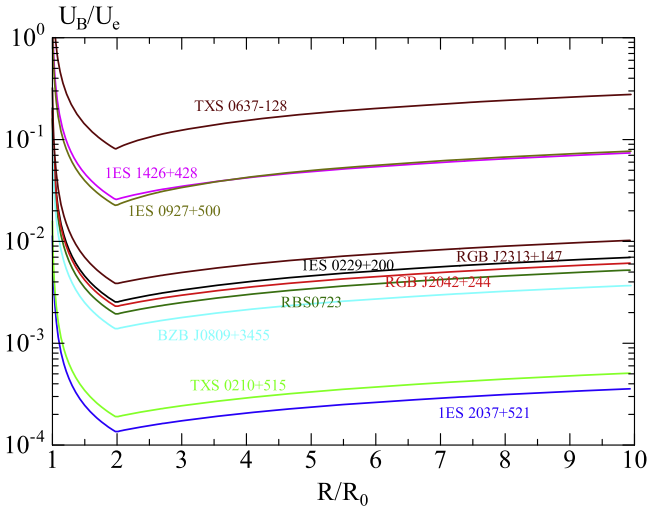

Figure 5. U_B/Ue distribution as a function of R/R_0 for the sources considered in this study in the SSC model (see Table 10 in Appendix E).

around 100 GeV (Figure 4(a)). To fit the spectrum without taking into account the MAGIC upper limits, the bulk Lorentz factor is adjusted to 10, while a hard electron spectrum ($p_1 = 1.5$) needs to be assumed to avoid the *Fermi* upper limits.

The MAGIC upper limits between 200 and 700 GeV constrain well the modeled spectrum for BZB J0809+3455 (Figure 4(b)). In this case, the model suggests that the synchrotron peak energy is below the peak energy criterion for EHBLs.

The soft X-ray spectrum in RGB J2313+147 (Figure 4(c)) also implies that this does not fall into the EHBL classification. The fitting result constrained by the MAGIC upper limits leads to $\varepsilon_{\rm syn,pk} \simeq 100$ eV.

For TXS 0637–128, we adopted the redshift $z = 0.136$ for our modeling (S. Paiano 2020, in preparation). The synchrotron spectral peak is produced by the electron cooling effect. The magnetization is the highest in our model samples, Figure 4(d).

The upper limits in the VHE range for RBS 0921 do not sufficiently constrain the model; therefore, the modeling of the broadband spectrum is omitted in this case. The SED is reported in Appendix F.

To summarize, the hard gamma-ray spectra seen in 1ES 0229+200, 1ES 1426+428, and 1ES 2037+521 were reproduced consistently with the spectral shape of the synchrotron component. Three different mechanisms were considered in the samples to form the synchrotron peak: the intrinsic break in the electron spectrum (1ES 0229+200, 1ES 0927+500, BZB J0809+3455, RGB J2313+147), the maximum electron energy (RBS 0723 and RGB J2042+244), and the cooling break (1ES 1426+428 and 1ES 2037+521). In general, we find that EHBLs have high values for $\gamma_{\rm br}$ or $\gamma_{\rm max}$ and a high synchrotron peak frequency $\nu_{\rm syn,pk}$, which implies that the Klein–Nishina effect is crucial. High-energy electrons interact mainly with photons with a much lower frequency than $\nu_{\rm syn,pk}$. The flux ratio of the two spectral components in EHBLs does not seem to be directly related to the magnetization parameter. According to the model, 1ES 0229+200 remains the source of the sample with the most extreme synchrotron peak, while RGB J2313+147 and BZB J0809+3455 are non-EHBL sources, having their peak below the defined threshold of 10^{17} Hz. Interestingly, the SED models of the remaining sources feature a synchrotron peak frequency in good agreement with the estimates of the 2WHSP reported in Table 1 with the exception of RGB J2313+147, whose peak was estimated at higher frequencies ($\nu_{\rm peak;2WHSP} = 10^{17.7}$ Hz, $\nu_{\rm peak;ssc} = 10^{16.5}$ Hz) and TXS 0210+515 whose SSC model predicts a much higher peak frequencies instead ($\nu_{\rm peak;2WHSP} = 10^{17.3}$ Hz, $\nu_{\rm peak;ssc} = 10^{18.3}$ Hz).

In our sample, in spite of the divergence in the model, the magnetization parameters U_B/U_e displayed in Figure 5 are commonly small. A comparison can be performed with Mrk 421, one of the most precisely observed blazars, where the magnetization has been estimated to be a few percent (Abdo et al. 2011; Asano & Hayashida 2018). The typical value of $\sim 10^{-3}$ found in the sample is much lower than that found in Mrk 421, implying a low magnetic field that is unfavorable for magnetic reconnection models (see, e.g., Sironi et al. 2015 and references therein). This also raises a contradiction with the magnetically driven jet model. Radio observations for the radio galaxy M87 revealed that the radio core region is dominated by the magnetic energy (Kino et al. 2015), and the bulk Lorentz factor and jet width profiles along the jet (Nakamura & Asada 2013) are consistent with a magnetically driven parabolic jet model (Komissarov et al. 2009). These observations support highly magnetized jet models, but the spectra in EHBLs may require either a fast dissipation of the magnetic field at the root of the jet or another jet acceleration model.

It should be noted that large error bars permit adopting different parameter sets. Therefore, R_0 was fixed to search for conservative parameters in this paper. The parameters in Table 10 in Appendix E are such examples. Moreover, considering the short variability in blazars, the GeV–TeV fluxes obtained with long integration times are not completely simultaneous with observations at other wavelengths. These uncertainties may change the interpretation, especially for the magnetization. In fact, in 1ES 2037+521, for example, another parameter set was found when implying $U_B/U_e \sim 10^{-5}$, different from the model presented in Figure 3(d). However, an extreme parameter set such as a very low magnetic field ($U_B/U_e \ll 10^{-3}$) or a very high $\gamma_{\rm min}$ is not necessarily required to fit the EHBL spectra in this paper.

7.2. Spine–Layer Model

The main outcome of the modeling of the sample of EHBLs with the SSC model presented in the previous section is a rather low magnetization. This is somehow in contradiction with the theoretical and observational constrain of equipartition needed to launch and sustain the jet close to the central massive black hole. As discussed in Tavecchio & Ghisellini (2015), a possibility for solving this problem is to decouple the synchrotron and IC components, assuming the existence of a supplementary source of soft photons intervening in the IC emission, as envisioned in the so-called spine–layer model (Ghisellini et al. 2005; Tavecchio & Ghisellini 2008). In this model, one assumes the existence of two regions in the jet: a faster inner core (the spine, with Lorentz factor Γ), surrounded by a slower sheath of material (the layer, with Lorentz factor $\Gamma_{\rm L}$). The radiation emitted by one region as observed in the frame of the other is amplified because of the relative motion. In this way, the IC luminosity of both components (in particular that of the spine) is increased with respect to that of the one-zone model. Given the larger radiation energy density with respect to the standard model, it is possible to increase the magnetic energy density (and decrease the electron energy density), thus reaching conditions close to equipartition.

In this scenario, the emission regions are filled with particles distributed in energy according to a smoothed broken power law:

$$N(\gamma) = K\gamma^{-n_1}\left(1 + \frac{\gamma}{\gamma_{\rm b}}\right)^{n_1-n_2}, \ \gamma_{\rm min} < \gamma < \gamma_{\rm max}. \qquad (5)$$

The distribution has normalization K between $\gamma_{\rm min}$ and $\gamma_{\rm max}$ and slopes n_1 and n_2 below and above the break, γ_b (Maraschi & Tavecchio 2003). This model requires specifying a relatively large number of parameters. To reduce the free parameters, the Lorentz factors of the spine and the layer are fixed to $\Gamma = 20$ and $\Gamma_{\rm L} = 3$, and the further assumption $\delta = \Gamma$ is made, thus fixing the viewing angle of the jet $\theta_v \simeq 2.^\circ 9$. Moreover, the minimum electron Lorentz factor of the spine is fixed to $\gamma_{\rm min} = 100$. The other parameters (in particular the luminosity of the layer emission) were varied so that the spine is close to equipartition.

This alternative scenario is tested on 1ES 0229+200 as well as on the four sources with significant detection with MAGIC and RGB J2042+244, for which a hint of a signal was found. For the remaining sources, we notice that without a detection at VHE, the parameters are not sufficiently constrained, and therefore, we do not further investigate the applicability of the spine–layer (and proton synchrotron; see later) model. The results of the model are displayed in Figure 3 by the black continuous line. In Table 11 in Appendix E, the parameters used for the spine are reported. As expected, the values of the magnetic field adopted in this model are higher than those assumed in the SSC model and in all, it is possible to obtain a satisfactory fit of the data assuming rough equipartition conditions. Because equipartition also marks the condition to have the lowest jet power required to have a given radiative output (e.g., Ghisellini & Celotti 2001), the jet powers estimated with the spine–jet scenario are systematically lower (by more than one order of magnitude) than those required by the SSC model.

7.3. Proton Synchrotron Scenario

The second alternative model considered is a scenario in which proton synchrotron radiation is responsible for the γ-ray component of the blazar SED. Blazar hadronic emission models have long been considered a valid alternative to leptonic models, in particular thanks to the natural link they provide with neutrino astronomy and ultra-HE cosmic-ray acceleration in AGN jets. One weakness of blazar hadronic models is that they require a rather large power in the protons responsible for the emission, often larger than the Eddington luminosity of the black hole powering the AGN. This is particularly true for bright FSRQs, as discussed, e.g., in Zdziarski & Böttcher (2015). For low-luminosity BL Lac objects, on the other hand, a proton synchrotron solution with a much lower, sub-Eddington, proton luminosity can be achieved, as discussed in Cerruti et al. (2015). In addition, the absence of fast variability in EHBLs, in contrast with that observed in typical HBLs, is also consistent with the slow cooling timescale of hadrons in the jet.

Similar to the spine–layer model case, the proton synchrotron model was tested only for the sources with a VHE gamma-ray spectrum determination. Without a spectral determination at VHE gamma-rays, in fact, the proton synchrotron component remains poorly constrained. Moreover, the number of free parameters of blazar hadronic models is much higher than the one of leptonic models, due to the extra proton energy distribution. In order to reduce the parameter space to study, some physically motivated assumptions are made:

1. The Doppler factor of the emitting region δ is fixed at 30, a value typical for blazars (Tavecchio et al. 2010) and consistent with the estimates from radio observations.
2. The size of the emitting region R is usually constrained by the observed variability timescale via the usual causality argument; given that for the majority of the sources no fast (dayscale or less) variability is seen at any wavelength, a $R \leqslant 1.6 \times 10^{17}\ (1+z)^{-1}$ cm is assumed. This value translates, for a Doppler factor $\delta = 30$, into a variability timescale of two days.
3. The minimum and break electron Lorentz factors are fixed at $\gamma_{e,\rm min} = \gamma_{e,\rm break} = 200$. The minimum proton Lorentz factor is fixed to $\gamma_{p,\rm max} = 1$, while the break proton Lorentz factor ($\gamma_{p,\rm break}$) is assumed to be equal to the maximum proton Lorentz factor ($\gamma_{p,\rm max}$).
4. The maximum proton Lorentz factor $\gamma_{p,\rm max}$ is constrained by equating the acceleration and cooling timescales: the acceleration timescale is expressed as $\tau_{acc} = (m_p c/\eta eB)\gamma_p$, where η is a parameter defining the efficiency of the acceleration mechanism, fixed to 0.1; the cooling timescales considered are the adiabatic one, $\tau_{\rm ad} \simeq 2R/c$, and the synchrotron one.
5. Hadrons and leptons share the same acceleration mechanism, and in particular, the power-law index of the injected particle distribution is identical, i.e., $\alpha_1 = \alpha_{e,1} = \alpha_{p,1}$ and $\alpha_2 = \alpha_{e,2} = \alpha_{p,2}$.
6. The lepton energy distribution at equilibrium is computed assuming that the main cooling mechanism is synchrotron radiation.

The proton synchrotron spectrum, with $\gamma_{p,\rm Max}$ constrained as defined above, is characterized by a clear degeneracy in the B–R plane, with solutions lying on a line $B \propto R^{-2/3}$ displaying the same peak frequency, being thus indistinguishable in the absence of additional information (i.e., neutrinos, or on the basis of their proton power). It exists in addition to a maximum peak frequency of the proton synchrotron component, which corresponds to the transition between the adiabatic-dominated and synchrotron-dominated cooling regimes (see Cerruti et al. 2015) and is equal to $1.28 \times 10^{26} \frac{1}{(1+z)} \frac{(3-\alpha_{p,1})}{1.5} \frac{\delta}{10}$ Hz.

A total of 175 hadronic models are produced, scanning the following parameter space: $\nu_{\rm syn,peak} \in [0.1\nu_{\rm Max}, \nu_{\rm Max}]$, $R \in [10^{14}{\rm cm}, R_{\rm Max}]$, and the proton normalization $K_p \in [K^\star/3, 3K^\star]$, where $K^\star$ corresponds to the proton density which provides a synchrotron spectrum at the level of the MAGIC spectra. Solutions which correctly describe the SED are selected via a χ^2 test, identifying a posteriori the solution with the lowest χ^2 and applying a $\Delta\chi^2$ cut corresponding to a 1σ interval. It is important to underline here that the χ^2 is computed without taking into account systematic uncertainties on the spectral measurements of the various instruments. The corresponding model parameters are provided in Table 12 in Appendix E, while the minimum-χ^2 proton synchrotron solutions are shown in Figure 3 together with the leptonic cases.

Proton synchrotron solutions provide a good description of the SEDs of extreme blazars, with luminosities which can be as low as 10^{45} erg s^{-1}, only a small fraction of the Eddington luminosity of the supermassive black hole powering the blazar, which is $1.26 \times 10^{47}\ (M/10^9 M_\odot)$ erg s^{-1}. One parameter which takes unusual values is the injection index of the particle distributions, which is very hard ($\alpha_{e,1} = \alpha_{p,1} = 1.1$–$1.3$) compared to the value expected from relativistic shock acceleration ($\alpha \simeq 2.2$). On the other hand, such hard values for the injection index can be compatible with particle acceleration by magnetic reconnection (see, e.g., Sironi & Spitkovsky 2014). It is important to underline, however, that the values of $\alpha_{e,1} = \alpha_{p,1}$ are not the result of the SED modeling, but are a direct consequence of the hypotheses of co-acceleration of electrons and protons and of simple synchrotron cooling as the main driver for the steady-state electron distribution. Relaxing these hypotheses can lead to softer values for $\alpha_{e,1}$ and $\alpha_{p,1}$, more in line with shock acceleration.

In Figure 3, together with the electromagnetic emission, we also show the neutrino emission, which appears in the

PeV–EeV band. The neutrino emission from all proton synchrotron models is rather moderate, showing a typical peak flux several orders of magnitudes lower than the gamma-ray peak. While the proton synchrotron model is degenerate in terms of photon emission, it predicts different neutrino fluxes as a function of the compactness of the emitting region (smaller and denser emitting regions resulting in a higher rate of proton–photon interactions, and thus neutrino production). The maximum neutrino flux expected from the proton synchrotron models for the six sources under study is shown in Appendix G. The most promising source in terms of neutrino output is 1ES 1426+428, which, due to the bright soft photon field that acts as a target for proton–photon interactions, can produce a neutrino flux peaking at 10^{-12} erg cm^{-2} s^{-1}. But even in this particular case, these neutrino fluxes remain out of reach for the current neutrino observatories such as IceCube. This result is consistent with the nondetection of extreme blazars as point-like PeV neutrino emitters. The fact that the proton synchrotron model is not associated with a significant neutrino emission is also in agreement with the theoretical results triggered by the recent detection of TXS 0506+056 as the counterpart of the HE neutrino IC 170922A (IceCube Collaboration et al. 2018; Gao et al. 2018; Keivani et al. 2018; Cerruti et al. 2019).

8. Conclusions

This paper reports the results of a multiyear observational campaign carried out by the MAGIC Collaboration and aimed at a detailed characterization of the SEDs of 10 EHBLs. The sources have been selected with different, complementary criteria and were observed with the MAGIC telescopes between 2010 and 2017. Observations of the archetypal EHBL 1ES 0229+200 between 2013 and 2017 were also included and used for comparison. Due to their relevance for the SED characterization in EHBLs, large part of the MAGIC data have been complemented by simultaneous *Swift*-XRT observations.

The analysis of 265 hr MAGIC data revealed a significant VHE gamma-ray signal from four sources: 1ES 1426+428, already detected by the HEGRA and VERITAS arrays, and the three new sources 1ES 2037+521, RBS 0723, and TXS 0210 +515. In addition, a hint of the VHE gamma-ray signal was found from RGB J2042+244. The intrinsic (EBL-corrected) spectra are on average quite hard, an indication of the extreme location of the second SED peak, exceeding the 100 GeV range. The faint gamma-ray fluxes prevented a detailed time-resolved analysis. Because the SED peaks are shifted toward high energies, EHBLs are by definition faint and usually hard *Fermi*-LAT sources. Except for RBS 0921, from which only a hint of the HE gamma-ray signal has been observed by *Fermi*-LAT, the spectral indices determined in time intervals centered on MAGIC observations range from 1.4 ± 0.2 to 1.9 ± 0.2. Once corrected for the EBL absorption, the spectral indices of the VHE gamma-ray spectra range from 1.6 ± 0.3 to 2.7 ± 1.2. This suggests a hard-TeV nature for all detected sources but RBS 0723, whose spectrum is affected by large error bars but still in agreement with the hard-TeV nature hypothesis. Among the new TeV-detected sources, TXS 0210 +515 is the source with the hardest spectral index, making it a good target for deep exposure observations.

In the soft X-ray band, the analysis of all the available *Swift*-XRT data, including archival data, suggested only a limited variability, within a factor of 2. The X-ray spectral indices are anticorrelated with the flux levels, in agreement with the harder-when-brighter behavior typical for other TeV BL Lac objects.

For two sources (TXS 0210+515 and RGB J2313+147), the available *NuSTAR* data were also analyzed, while the *NuSTAR* data of 1ES 0229+200 covering the MAGIC data window were adopted from literature. With its 3.0–79 keV energy coverage, *NuSTAR* is the ideal instrument to study and characterize EHBLs, even better if the data are analyzed in conjunction with the *Swift*-XRT data, allowing us to have a simultaneous fit of the X-ray spectrum from 0.5 to 79 keV (see Appendix B). In the case of TXS 0210+515, a clear evidence for a curved X-ray spectrum was found. The spectrum is well described by a log-parabola model, suggesting a position of the synchrotron peak at 7.1 ± 1.1 keV. This confirms the extreme synchrotron nature of the source, similar to (but still less extreme than) 1ES 0229+200, for which a synchrotron peak at 9.1 ± 0.7 keV has been estimated by Costamante et al. (2018). For RGB J2313+147, the X-ray flux observed with *NuSTAR* is a factor of 10 lower with respect to that of TXS 0210+515. The joint XRT and *NuSTAR* data are compatible with a power-law spectrum with index larger than 2 and suggest a synchrotron peak located below 10^{17} Hz. This source was therefore very likely a standard HBL and not an EHBL during the observations.

All of the SEDs were modeled with the single-zone, conical jet SSC model described by Asano & Hayashida (2018 and references therein). The six sources with spectral determination at VHE gamma-rays, i.e., the four MAGIC detections, the hint-of-a-signal source, and the reference source 1ES 0229+200, were also modeled with two alternative scenarios: a leptonic scenario with a structured jet, the spine–layer model (Ghisellini et al. 2005), and the proton synchrotron model described by Cerruti et al. (2015). All of the models provide a good description of the quasi-simultaneous multiwavelength observational data. However, the resulting parameters differ substantially in the three scenarios.

The main conclusion of the single-zone, conical jet SSC model applied to our data is that it requires a critically low magnetization, in tension with radio observations of nearby radio galaxies. The spine–layer model seems to provide a satisfactory solution to the magnetization problem, resulting in a quasi-equipartition of the magnetic field and matter in the emission zone. The proton synchrotron model, instead, while still providing a good fit to the multiwavelength data, results in a highly magnetized jet, still far from equipartition. Therefore, with the current data set we cannot favor or disfavour any model considered.

Future observations of the EHBLs presented in this work (and of other EHBLs) will be essential for testing the emission models. Probing fast variability at VHE and variability at different frequencies, in particular between the X-ray and VHE bands, is likely the most powerful tool at our disposal to test emission models. But given the faint signal at VHE with respect to the spectral capabilities of the current generation of IACTs, this is mostly a target for telescopes of future generations. In the meantime, coordinated multifrequency monitoring and discovery of new VHE emitters belonging to the EHBL class are essential to prepare the ground for future discoveries.

The authors are grateful to Luigi Costamante for providing the data previously published. Part of this work is based on

archival data, software, or online services provided by the Space Science Data Center—ASI. This research has made use of data and/or software provided by the High Energy Astrophysics Science Archive Research Center (HEASARC), which is a service of the Astrophysics Science Division at NASA/GSFC and the High Energy Astrophysics Division of the Smithsonian Astrophysical Observatory.

We would like to thank the Instituto de Astrofísica de Canarias for the excellent working conditions at the Observatorio del Roque de los Muchachos in La Palma. The financial support of the German BMBF and MPG, the Italian INFN and INAF, the Swiss National Fund SNF, the ERDF under the Spanish MINECO (FPA2015-69818-P, FPA2012-36668, FPA 2015-68378-P, FPA2017-82729-C6-2-R, FPA2015-69210-C6-4-R, FPA2015-69210-C6-6-R, AYA2015-71042-P, AYA2016-76012-C3-1-P, ESP2015-71662-C2-2-P, FPA2017-90566-REDC), the Indian Department of Atomic Energy, the Japanese JSPS and MEXT, the Bulgarian Ministry of Education and Science, National RI Roadmap Project DO1-153/28.08.2018, and the Academy of Finland grant nr. 320045 is gratefully acknowledged. This work was also supported by the Spanish Centro de Excelencia "Severo Ochoa" SEV-2016-0588 and SEV-2015-0548, and Unidad de Excelencia "María de Maeztu" MDM-2014-0369, by the Croatian Science Foundation (HrZZ) Project IP-2016-06-9782 and the University of Rijeka Project 13.12.1.3.02, by the DFG Collaborative Research Centers SFB823/C4 and SFB876/C3, the Polish National Research Centre grant UMO-2016/22/M/ST9/00382, and by the Brazilian MCTIC, CNPq and FAPERJ.

E.P. has received funding from the European Union's Horizon 2020 research and innovation programme under the Marie Sklodowska–Curie grant agreement No. 664931.

M.C. has received financial support through the Postdoctoral Junior Leader Fellowship Programme from la Caixa Banking Foundation, grant No. LCF/BQ/LI18/11630012.

Software: MARS (Zanin 2013), enrico (Sanchez & Deil 2014), nustardas (v1.7.1) (https://heasarc.gsfc.nasa.gov/docs/nustar/analysis).

Appendix A
MAGIC Data Analysis Details

MAGIC (Aleksić et al. 2016a) is a system of two IACTs designed to collect the UV-optical Cherenkov light generated when a gamma-ray enters the atmosphere, producing a shower of superluminal, charged particles. The two telescopes are located on the Canary island of La Palma, at 2200 m altitude. With their large reflective surface of 17 m diameter each, the MAGIC telescopes are designed to reach an energy threshold as low as 50 GeV when operated in standard trigger mode. Above 220 GeV, the integral sensitivity for point-like sources is $(0.66 \pm 0.03)\%$ of the Crab Nebula flux in 50 hr observations, assuming a Crab Nebula–like spectrum. The angular resolution at those energies is below $0.^{\circ}07$, while the energy resolution is 16%. The performance of the instruments and the details of the data analysis are fully described in Aleksić et al. (2016b).

The main parameters influencing the energy threshold of the analysis are the zenith angle of the observations and the background light conditions during data taking. Medium and high zenith angle observations (above 35° and above 50°, respectively) are characterized by an increased energy threshold, due to the passage of the particle showers through a larger layer of atmosphere, but also due to an increased sensitivity at the highest energies related to the enlarged effective area (Aleksić et al. 2016b).

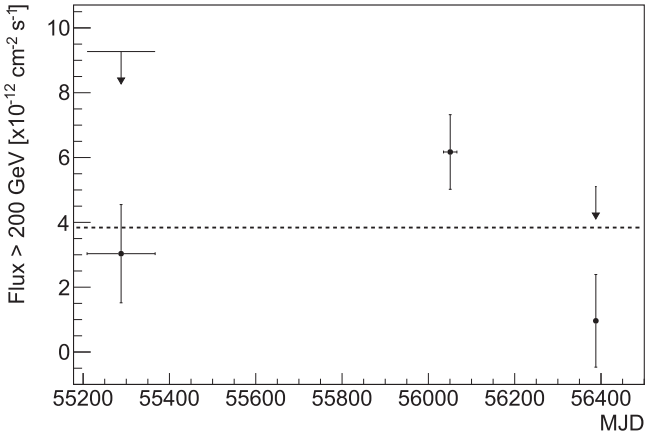

Figure 6. 1ES 1426+428 multiyear MAGIC VHE gamma-ray light curve above 200 GeV between 2011 and 2013. Black downward-pointing arrows correspond to 95% confidence upper limits, which were computed for the observations where the interval of the measured flux (black points) ± twice the error contains zero.

A higher level of background light due to the presence of the Moon strongly affects the energy threshold of the analysis. However, the performance of the telescope system remains unaffected as long as the intensity of the moonlight is not too high (MAGIC Collaboration et al. 2017b). The data were analyzed using the MAGIC analysis and reconstruction software package (Zanin 2013) that was adapted for stereoscopic observations (Moralejo et al. 2009). To look for a significant VHE gamma-ray excess, a standard variable, named θ^2, which is defined as the squared angular distance of the reconstructed shower direction with respect to the source location in the camera, was used. The typical signature of VHE gamma-rays is peaking at low θ^2 values, i.e., in the so-called "On" region in the camera, over the normalized cosmic-ray background, which is estimated from three equivalent "Off" regions, located at 90°, 180°, and 270° with respect to the reconstructed source position in the camera.

In Figure 6, the multiyear light curve of 1ES 1426+428 is displayed, reporting the average values measured from the 2010, 2012, and 2013 observations. Only in 2012 was the source detected with a significance larger than 5σ, as reported in Table 2. The average flux above 200 GeV is $(3.84 \pm 0.77) \times 10^{-12}\,\mathrm{cm}^{-2}\,\mathrm{s}^{-1}$. From these data, the hypothesis of a constant flux cannot be excluded, especially if we take into account the systematic uncertainty on the integral flux.

A comparison of previous VHE gamma-ray observations based on the observed spectral indices, the differential fluxes at a given energy, and the integral fluxes for a common energy range was performed (see Table 5). The observed spectral indices are consistent within their statistical errors. The comparison of the differential and integral fluxes is based on the power-law fits to the observed differential spectra. The decorrelation energy of the spectral analysis of this work and an energy threshold of 200 GeV were used for the differential and integral flux calculations, respectively. The statistical errors reported for the flux calculations are overestimated as, for simplicity, the uncertainties of the fit parameters were considered to be uncorrelated when propagating the errors. On the other hand, the systematic uncertainties of the different

Table 5
Comparison of the MAGIC Results of 1ES 1426+428 from This Work with Previous VHE Gamma-ray Observations of this Source

Year	Energy range (GeV)	F_0 $\times 10^{-12}$(cm^{-2} s^{-1} TeV^{-1})	$\Gamma_{\rm obs}$	$F_{E=242\,\rm GeV}$ $\times 10^{-12}$(cm^{-2} s^{-1} TeV^{-1})	$F_{(200<E<5000)\,\rm GeV}$ $\times 10^{-12}$(cm^{-2} s^{-1})
1998–2000[a]	250–1000	$67 \pm 13_{E=400\,\rm GeV}$	3.6 ± 0.6	411 ± 141	63 ± 16
1999–2000[b]	700–10,000	$2.0 \pm 1.3_{E=1000\,\rm GeV}$	2.6 ± 0.6	80 ± 86	16 ± 14
2001[c]	250–1700	$4.9 \pm 1.4_{E=1000\,\rm GeV}$	3.5 ± 0.4	703 ± 352	110 ± 47
2012[d]	100–1700	$25.6 \pm 0.1_{E=242\,\rm GeV}$	2.6 ± 0.3	25.6 ± 0.1	5.2 ± 0.7

Notes. Columns from left to right: year(s) of observation, energy range, fit parameters of the observed spectra, i.e., the flux normalization and the spectral index, differential flux and integral flux derived from the simple power-law fits. Only the statistical errors are reported.
[a] Djannati-Ataï et al. (2002).
[b] Aharonian et al. (2003).
[c] Petry et al. (2002).
[d] This work; the integral flux reported here is calculated from the spectral fit and thus shows little variation from the averaged flux observed in 2012 (see Figure 6), whose calculation is based on the number of gamma-like excess events instead. However, within the statistical errors, both values are consistent.

instruments, which have been ignored in this comparison, might dominate over the statistical errors. It also has to be noted that the VHE gamma-ray spectra were determined for different energy ranges, which introduces a certain bias in the flux comparison. Given all of these circumstances, a clear conclusion on the variability of the VHE gamma-ray flux of 1ES 1426+428 could not be drawn.

Appendix B
Fermi-LAT Data Analysis Details

The *Fermi*-LAT (Atwood et al. 2009) is a pair conversion telescope consisting of a 4 × 4 array of silicon strip trackers and tungsten converters and a cesium-iodine-based calorimeter. The instrument is fully covered by a segmented anti-coincidence shield, which provides a highly efficient vetoing against charged particle background events. The LAT is sensitive to gamma-rays from 20 MeV to more than 300 GeV and normally operates in survey mode, covering the whole sky every three hours and providing an instantaneous field of view of 2.4 sr.

The LAT data were extracted from the weekly LAT data files available in the FSSC data center.[42] For each data sample, only Pass 8 source-class photons detected within 15° of the nominal position of the analyzed source were considered. Only events whose reconstructed energy lies between 1 GeV and 300 GeV were selected. The relatively high energy threshold was set to simplify the analysis of the two fields and remove contamination from secondary sources. This was particularly important in the case of 1ES 2037+502 due to its proximity to the galactic plane. Following the event selection recommendations from Cicerone,[43] only good data (`(DATA_QUAL>0)&&(LAT_CONFIG==1)`) with zenith distance lower than 90° were included.

For each data sample, the data were reduced and analyzed using the open-source software package `enrico` (Sanchez & Deil 2014) as a wrapper for the *Fermi* `ScienceTools` (version v10r0p5).[44] A summed binned likelihood analysis approach was followed, splitting PSF event types (0, 1, 2 and 3) with 10 bins per energy decade and using the instrument response functions P8R2_SOURCE_V6. All of the 3FGL sources within the region of interest are included in the model, along with Galactic and isotropic models using `gll_iem_v06.fits` and `iso_P8R2_SOURCE_V6_v06.txt` files, respectively. The spectra of the sources were selected such as to maximize the value of the likelihood while being physically sound, following the same method described in MAGIC Collaboration et al. (2019b). All sources were modeled with attenuated spectral shapes using the EBL template from Franceschini et al. (2008). For each analysis, the spectral parameters of all sources that are significantly detected within a radius of 3° around the source of interest were left free in the fit in order to account for their possible variability. The parameters of the rest of the sources are fixed to the published 3FGL values. The normalization of the diffuse components was left free.

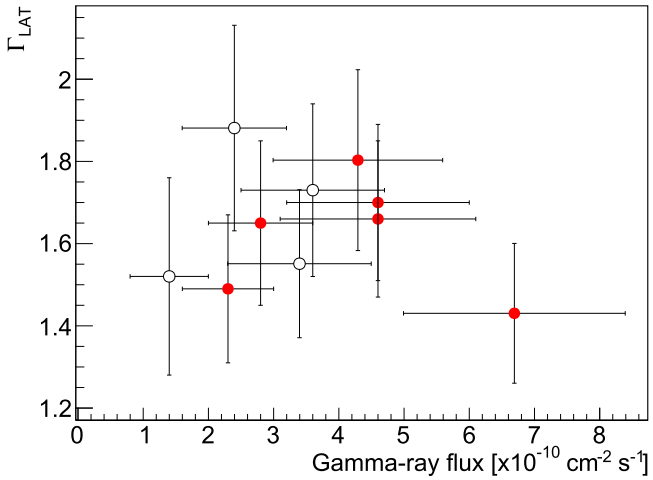

Figure 7. Correlation study between the spectral index describing the average spectrum in the HE gamma-ray band and the integral HE gamma-ray flux between 1 and 100 GeV, both reported in Table 6. Filled and open circles refer to sources detected and not detected at VHE gamma-rays, respectively. The hint-of-a-signal source is considered here among the detected sources.

In order to investigate the relation of the *Fermi*-LAT spectral properties on the extremeness at VHE, we have compared the LAT spectral index and flux reported in Table 4 for MAGIC-detected and -undetected sources (a similar study for the X-ray band is reported above). Our data, displayed in Figure 7, show that while the LAT spectral index does not have any effect on the detection probability, the flux seems to have a role: of the five detected sources, three were the brightest in the GeV band. This is quite regular and does not constitute a valid criterion for

[42] https://fermi.gsfc.nasa.gov/ssc/data/access/
[43] https://fermi.gsfc.nasa.gov/ssc/data/analysis/documentation/Cicerone/
[44] http://fermi.gsfc.nasa.gov/ssc/data/analysis/scitools

Table 6
Main Spectral Parameters from the 3FGL, 2FHL, and 3FHL Catalogs

Source	$\text{Flux}_{3\text{FGL}}$ (1–100 GeV) $\times 10^{-10}$ (photon cm^{-2} s^{-1})	$\Gamma_{3\text{FGL}}$	Significance (σ)	$\Gamma_{3\text{FHL}}$ $E > 10$ GeV	$\Gamma_{2\text{FHL}}$ $E > 50$ GeV
TXS 0210+515	4.17 ± 0.85	2.04 ± 0.17	7.2	1.55 ± 0.22	1.85 ± 0.47
TXS 0637–128	3.34 ± 0.93	1.51 ± 0.16	8.0	1.63 ± 0.18	1.63 ± 0.43
BZB J0809+3455	3.21 ± 0.68	1.67 ± 0.13	8.0	1.71 ± 0.27	1.09 ± 0.61
RBS 0723	5.06 ± 0.85	1.74 ± 0.11	10.5	1.86 ± 0.21	3.60 ± 1.27
1ES 0927+500	1.83 ± 0.68	1.45 ± 0.21	5.1	1.97 ± 0.32	N.A.
RBS 0921	N.A.	N.A.	N.A.	N.A.	N.A.
1ES 1426+428	6.60 ± 0.84	1.57 ± 0.08	16.7	1.91 ± 0.14	3.34 ± 0.58
1ES 2037+521	3.93 ± 0.13	1.89 ± 0.21	5.2	N.A.	N.A.
RGB J2042+244	5.15 ± 0.96	1.87 ± 0.14	8.4	1.88 ± 0.25	N.A.
RGB J2313+147	6.21 ± 0.97	1.76 ± 0.11	11.7	2.08 ± 0.24	3.56 ± 1.31
1ES 0229+200	4.39 ± 0.90	2.02 ± 0.15	7.2	N.A.	N.A.

Note. Columns from left to right: source name; HE gamma-ray flux in the range of 1–100 GeV, spectral index for the power-law fit in range of 100 MeV–100 GeV, and the detection significance reported by 3FGL (Acero et al. 2015); spectral index for the power-law fit >10 GeV reported in 3FHL (Ajello et al. 2017); spectral index for the power-law fit >50 GeV reported in 2FHL (Ackermann et al. 2016).

hard-TeV source selection (if the source is bright in LAT, it is more likely to be detected also in the VHE range). Interestingly, 1ES 0229+200 is instead the second faintest source of the sample in the GeV range. For comparison, the 3FGL, 2FHL (Ackermann et al. 2016), and 3FHL (Ajello et al. 2017) values are reported in Table 6.

Appendix C
Swift-XRT Data Analysis Details

For the *Swift*-XRT data analysis of each source, the multiepoch event list obtained by the XRT were downloaded from the publicly available SWIFTXRLOG (*Swift*-XRT Instrument Log[45]) for both photon-counting (PC) and window-timing (WT) modes. The standard *Swift*-XRT analysis procedure is described by Evans et al. (2009). The PC data were processed using the procedure described by Fallah Ramazani et al. (2017). For the WT observation data, a box with a length of 40 pixels at the center of the source and aligned to the telescope roll angle was defined for the source region. The background region is defined by a box with a length of 40 pixels aligned to the telescope roll angle and 100 pixels away from the center of the source.

There are open issues for analyzing the XRT data,[46,47] such as faults in the silicon crystalline structure of the *Swift*-XRT CCD. These open issues mostly affect the data obtained with WT mode. However, some of them (charge traps) still can affect the spectra observed during PC mode. In order to address these issues systematically in our data analysis, for both modes of observation using the χ^2 likelihood method, the spectra of each observation were fitted assuming all possible combination of pixel-clipping patterns (XRT Grades) and point-spread-function (XRT response matrix files; Burrows et al. 2005). Simultaneously, two mathematical models (i.e., power law and log parabola; Massaro et al. 2004) and the fixed equivalent Galactic hydrogen column density reported by Kalberla et al. (2005) are assumed during the spectral-fitting procedure. The spectra are fitted in the range of 0.3–10 keV except for the spectra of 1ES 2037+521. For 1ES 2037+521, the spectra is heavily absorbed by Galactic extinction at energies below 1.5 keV. The current method, which is used in the data analysis chain, cannot address this issue correctly (Willingale et al. 2013). Therefore, we used 1.5–10 keV as the energy range of the spectral fitting for 1ES 2037+521. In total, for each observation, 6 and 16 spectra (PC and WT modes accordingly) are compared to each other, and the best fitted model which describes the observation data is selected. Equivalent Galactic hydrogen column densities of the sources are presented in Table 1.

Table 7 reports an example of the results obtained from *Swift*-XRT data. A small part of this sample was available in the public database, while the large majority of the observations was requested via ToO by the MAGIC team that performed quasi-simultaneous pointings with MAGIC telescopes. It is notable that the fit statistics are poor (i.e., $1.9 <$ reduced-$\chi^2 < 2.0$) for a few of the observations (e.g., Table 7, OBS ID 00046559005) due to the bad quality of raw data. In Table 8, the results of combining all the *Swift*-XRT data during MAGIC observation window for each are shown. The left panel of Figure 8 illustrates the distribution of X-ray photon indices obtained from combined data sets in the index–flux plane for the detected (solid circle) and nondetected (open circles) sources in VHE gamma-rays. No clear relation between the flux or the index and the detection probability at VHE gamma-rays is evident (Figure 8, right panel).

[45] https://heasarc.gsfc.nasa.gov/W3Browse/all/swiftxrlog.html
[46] http://www.swift.ac.uk/analysis/xrt/digest_cal.php
[47] http://www.swift.ac.uk/analysis/xrt/rmfs.php

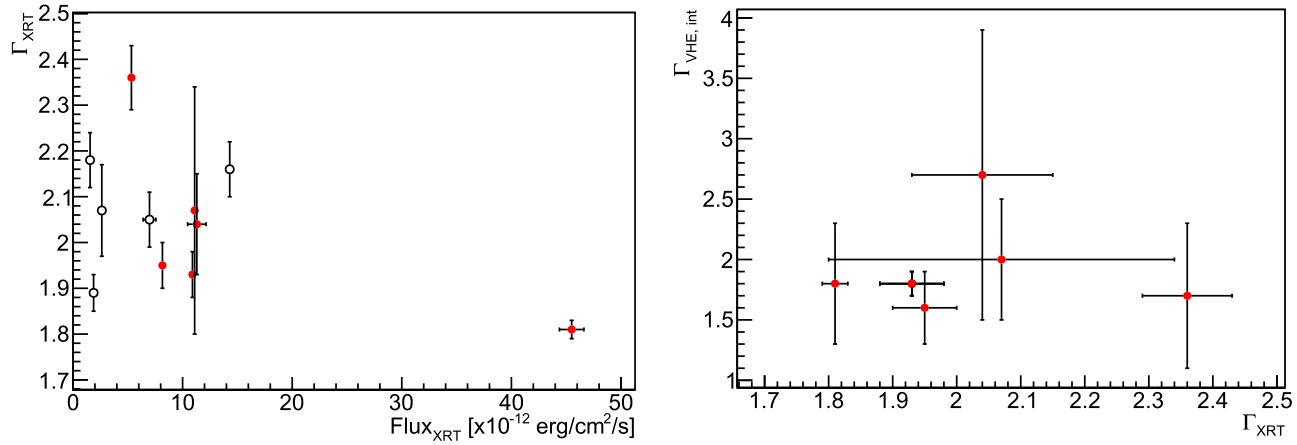

Figure 8. Left: X-ray power-law index vs. integral flux (2–10 keV) from the analysis of the average *Swift*-XRT spectra during MAGIC data taking, as reported in Table 8. Filled red markers are sources detected at VHE, while open markers represent sources still undetected at VHE. The hint-of-a-signal source is considered here among the detected sources. Right: power-law index in the X-ray band, from Table 8, and the power-law index of the EBL-corrected (intrinsic) spectrum measured in the VHE gamma-ray band, reported in Table 3.

Table 7
Example of the *Swift*-XRT Results for RGB J2042+244

Day	OBS ID	Exposure	Power Law		Log-parabola			Prob.[a]	Flux	
			Γ	χ^2/dof	Γ	β	χ^2/dof		$F_{2-10\,\mathrm{keV}}$	$F_{0.3-10\,\mathrm{keV}}$
(MJD)		(s)						%	($\times 10^{-12}$ erg cm^{-2} s^{-1})	
55939.73	00046559001	3024	2.05 ± 0.07	28.2/28				0.7	4.7 ± 0.5	8.4 ± 0.5
56299.56	00046559002	1176	1.75 ± 0.18	5.2/4				47.0	4.1 ± 1.1	6.1 ± 1.0
57192.04	00046559003	1985	1.93 ± 0.07	29.5/27				99.6	9.2 ± 0.8	15.1 ± 0.9
57194.08	00046559004	1641	1.95 ± 0.08	17.5/22				67.1	8.6 ± 0.8	14.3 ± 1.0
57196.08	00046559005	1791	1.87 ± 0.07	50.9/26				19.1	9.8 ± 1.0	15.6 ± 1.0
57968.03	00046559006	1558			1.85 ± 0.12	0.98 ± 0.30	15.2/20	0.1	5.1 ± 0.7	12.0 ± 0.9
57979.33	00046559008	767	2.2 ± 0.24	2.9/3				66.2	6.7 ± 2.4	13.8 ± 3.0
57980.05	00046559009	1391	1.87 ± 0.07	35.4/25				36.7	12.4 ± 1.1	19.7 ± 1.1
57994.68	00046559010	787	2.03 ± 0.09	21.0/17				47.5	11.3 ± 1.4	19.7 ± 1.4
57996.94	00046559011	1371	2.01 ± 0.08	32.1/21				3.1	8.1 ± 0.8	14.0 ± 0.9

Notes. Columns from left to right: day, observation ID, exposure time, spectral index of power-law model, χ^2/dof of the fitted power-law model, spectral index of the log-parabola model, curvature parameter of the fitted log-parabola model, χ^2/dof of the log-parabola model, probability of the null-hypothesis of the F-test, X-ray flux in the range of 2–10 keV, and X-ray flux in the range of 0.3–10 keV.
[a] The log-parabola model is preferred over the power-law model with a 3σ confidence level if the F-test probability value is <0.27%.

(This table is available in its entirety in machine-readable form.)

Table 8
Main Spectral Parameters Resulting from Combining All *Swift*-XRT Pointings during the MAGIC Observation Window

Source	Interval (MJD)	$F_{(2-10\,\mathrm{keV})}$ ($\times 10^{-12}$ erg cm^{-2} s^{-1})	Γ	β	χ^2/dof	Γ_{Equi}
TXS 0210+515	57370–58042	8.16 ± 0.13	1.69 ± 0.02	0.23 ± 0.04	397.6/377	1.95 ± 0.05
TXS 0637–128	57775–58023	14.32 ± 0.32	1.71 ± 0.03	0.40 ± 0.05	351.6/320	2.16 ± 0.06
BZB J0809+3455	57012–57317	1.88 ± 0.09	1.89 ± 0.04		89.6/79	
RBS 0723	56629-56985	11.30 ± 0.84	1.63 ± 0.04	0.36 ± 0.09	89.7/101	2.04 ± 0.11
1ES 0927+500	55641–55649	6.98 ± 0.58	2.05 ± 0.06		47.6/36	
RBS 0921	57404–57483	2.63 ± 0.11	1.68 ± 0.04	0.34 ± 0.08	137.9/122	2.07 ± 0.10
1ES 1426+428	56039–56065	45.49 ± 1.12	1.81 ± 0.02		262.4/260	
1ES 2037+521[a]	57658–57672	11.13 ± 0.03	1.46 ± 0.17	0.54 ± 0.18	183.8/205	2.07 ± 0.27
RGB J2042+244	57194–58055	5.33 ± 0.15	2.01 ± 0.03	0.31 ± 0.06	210.9/219	2.36 ± 0.07
RGB J2313+147	57172	1.56 ± 0.13	2.18 ± 0.06		30.5/32	
1ES 0229+200	56566–57752	10.93 ± 0.25	1.50 ± 0.02	0.38 ± 0.04	320.8/327	1.93 ± 0.05

Notes. Columns from left to right: source name, time interval of observation(s), X-ray flux in the range of 2–10 keV, spectral index, curvature parameter of the log-parabola model, fit statistics, and equivalent spectral index when the log parabola is the best-fit model.
[a] The range for spectral analysis is 1.5–10 keV (see text for details).

Appendix D
NuSTAR Data Analysis Details

The level 1 data products were processed with the *NuSTAR* Data Analysis Software (`nustardas`) package (v1.7.1). Cleaned-event files (level 2 data products) were produced and calibrated using standard filtering criteria with the `NUPIPELINE` task, version 20180312 of the calibration files available in the *NuSTAR* CALDB and the OPTIMIZED parameter for the exclusion of the South Atlantic Anomaly passages.

For both objects, the source spectra were extracted from the cleaned-event files using a circle of 25 pixel ($\sim 60''$) radius, while the background was extracted from two distinct nearby circular regions of 30 pixel ($\sim 70''$) radius. The ancillary response files were generated with the `numkarf` task, applying corrections for the point-spread-function losses, exposure maps, and vignetting. The spectra were rebinned with a minimum of 20 counts per energy bin to allow for χ^2 spectral fitting.

Table 9 summarizes the results of the spectral analysis, described in the main text. The combined *NuSTAR* and *Swift*-XRT spectra are reported in Figure 9.

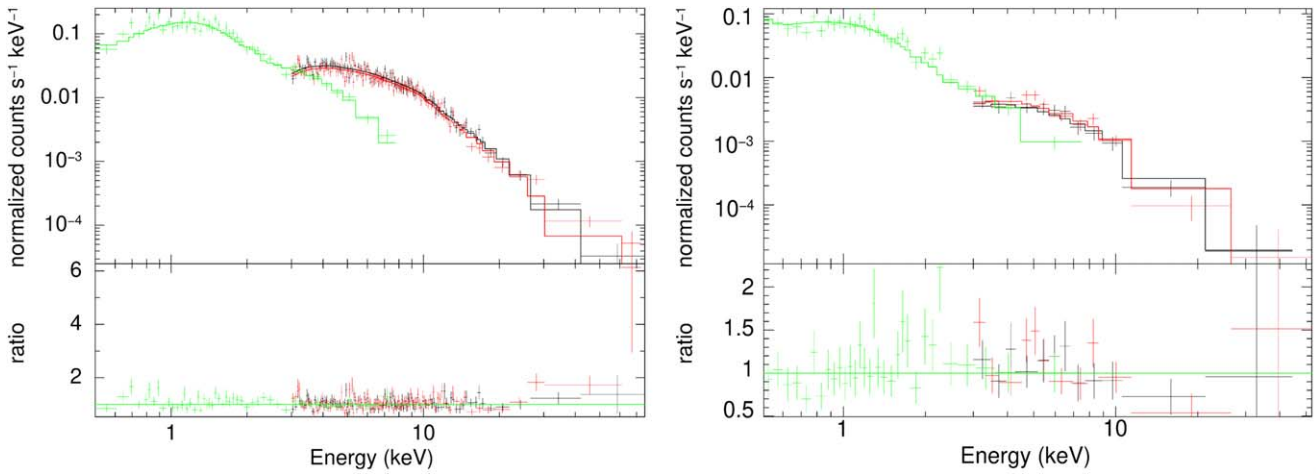

Figure 9. Left: *NuSTAR* (black, FPMA, and red, FPMB, points) and *Swift*-XRT (green points) spectra and residuals for TXS 0210+515 collected on 2016 January 30 simultaneously fitted with a log-parabola model. Right: *NuSTAR* (red and black points) and *Swift*-XRT (green points) spectra and residuals of RGB 2313+147 collected on 2015 May 30 simultaneously fitted with a power-law model.

Table 9
Summary of Fits to the 0.5–79 keV *Swift*-XRT + *NuSTAR* Spectrum of TXS 0210+515 and RGB J2313+147

Model	Parameter	TXS 0210+515	RGB 2313+147
Power law	Γ	1.96 ± 0.03	2.32 ± 0.10
	Flux (0.5–79 keV)	$(2.17^{+0.03}_{-0.04}) \times 10^{-11}$	$(2.17^{+0.12}_{-0.16}) \times 10^{-12}$
	χ^2/dof	387/311	62/63
Log Parabola	α	1.85 ± 0.04	$2.37^{+0.11}_{0.10}$
	β	0.20 ± 0.06	$0.35^{+0.18}_{-0.16}$
	E_0	3 keV (fixed)	3 keV (fixed)
	Flux (0.5–79 keV)	$(1.92^{+0.06}_{-0.02}) \times 10^{-11}$	$(1.90^{+0.14}_{-0.11}) \times 10^{-12}$
	χ^2/dof	348/310	50/62
	$\log \nu_{\rm synch}$	18.24 ± 0.07	17.33 ± 0.16

Note. Fits also included absorption fixed at the Galactic value. Flux and synchrotron peak frequency are given in units of erg cm^{-2} s^{-1} and Hz, respectively.

Appendix E
SED Parameters

In this section, the SED model parameters are reported in detail for the three adapted scenarios. Only the parameters which are left to vary are reported here. The fixed parameters are described in Section 7. The results of the single-zone, conical jet model for all of the sources of the study are listed in Table 10. Table 11 presents the parameters of the spine–layer model for the sources with a spectral determination, and Table 12 those of the proton synchrotron model. In the former case, the solution is degenerate and a range is proposed for some of the parameters.

Table 10
Model Parameters and Obtained Physical Values for the SSC Conical Jet Scenario

Source name	$\gamma_{\rm br}$ ($\times 10^5$)	$\gamma_{\rm max}$ ($\times 10^6$)	p_1	p_2	B_0 (G)	$L_e \times 10^{44}$ (erg s^{-1})	Γ	$\log(\nu_{\rm syn,pk})$[a] (Hz)	$\log(\nu_{\rm IC,pk})$[a] (Hz)	CD[a,b]	U_B/U_e[a] ($\times 10^{-3}$)	VHE?
TXS 0210+515	10.0	20.0	2.5	3.0	0.04	6.50	20	18.3	25.7	0.18	0.19	Y
TXS 0637–128	5.0	20.0	1.8	3.0	0.25	0.80	10	17.7	25.4	0.2	81.00	N
BZB J0809+3455	1.0	3.0	1.8	3.0	0.04	0.89	10	16.4	25.4	0.84	1.40	N
RBS 0723	⋯	2.0	2.2	⋯	0.11	4.90	20	18.1	25.8	0.37	1.90	Y
1ES 0927+500	3.0	3.0	1.5	2.5	0.13	0.71	10	17.6	25.9	0.25	23.00	N
1ES 1426+428	⋯	2.0	2.0	⋯	0.20	1.30	20	18.2	25.8	0.14	26.00	Y
1ES 2037+521	⋯	2.0	2.1	⋯	0.02	2.30	20	18.1	26.4	0.33	0.14	Y
RGB J2042+244	⋯	0.3	2.0	⋯	0.07	1.80	20	17.1	25.6	0.36	2.30	H
RGB J2313+147	0.8	20.0	2.0	3.5	0.09	1.60	20	16.5	25.3	0.37	3.90	N
1ES 0229+200	10.0	300.0	1.9	3.0	0.06	1.10	20	18.6	26.6	0.13	2.50	Y

Notes. Columns from left to right: source name, break and maximum electron Lorentz factor, spectral index of the electron energy distribution below and above γ_{br}, magnetic field, electron luminosity, bulk Lorentz factor of the jet, synchrotron and IC peak frequency resulting from the model, Compton dominance parameter, ratio between the magnetic and electron energy density evaluated at the radius where the electron injection shuts down, and the source detection status at VHE gamma-rays (Y: detected, N: not detected, and H: hint of signal).
[a] These quantities are derived quantities and not model parameters.
[b] The ratio of νL_ν at the IC peak to that at the synchrotron peak.

Table 11
Model Parameters and Obtained Physical Values for the Spine–Layer Scenario for the Sources with a VHE Gamma-Ray Spectral Determination

Source Name	γ_b ($\times 10^4$)	$\gamma_{\rm max}$ ($\times 10^6$)	n_1	n_2	B (G)	K (cm^{-3})	$R \times 10^{15}$ (cm)	U_B/U_e[a]	L_j[a] $\times 10^{42}$ (erg s^{-1})
TXS 0210+515	33.0	0.8	1.40	2.30	0.15	25.0	5.1	1.25	2.50
RBS 723	0.3	0.8	1.40	2.30	0.35	15.0	5.1	1.17	14.60
1ES 1426+428	3.0	2.0	1.40	2.90	0.34	3.5	7.1	1.07	20.50
1ES 2037+521	13.0	2.0	1.40	3.00	0.40	2.9	1.3	0.75	0.97
RGB J2042+244	2.0	2.0	1.40	2.95	0.30	3.0	4.8	1.21	7.00
1ES 0229+200	13.0	6.0	1.40	3.40	0.40	2.6	3.2	0.74	6.30

Notes. Columns from left to right: source name, break and maximum electron Lorentz factor, spectral index of the electron energy distribution below and above γ_b, magnetic field, normalization of the electron distribution, radius of the emission zone, ratio between the magnetic and electron energy densities of the layer, and kinetic luminosity of the jet.
[a] These quantities are derived quantities, and not model parameters.

Table 12
Model Parameters and Obtained Physical Values for the Hadronic Scenario for the Sources with a VHE Gamma-Ray Spectral Determination

Source Name	$\gamma_{e,\max}$ ($\times 10^4$)	α_1	α_2	B (G)	$K_e \times 10^{-3}$ (cm^{-3})	$R \times 10^{14}$ (cm)	$\gamma_{p,\max}$ ($\times 10^9$)	η (erg cm^{-3})	u_B[a] ($\times 10^{-5}$)	u_p/u_B[a] ($\times 10^{-5}$)	L[a,b] $\times 10^{46}$ (erg s^{-1})
TXS 0210+515	1.0–15.9	1.30	2.30	1.9–468	0.002–4890	1–1480	1.7–48.9	0.06–4.9	0.15–8710	0.008–47.8	0.10–48.1
RBS 0723	1.1–16.5	1.25	2.25	2.1–468	0.035–68640	1–1300	1.6–28.0	0.12–3.5	0.18–8710	1.1–1300	0.10–32.4
1ES 1426+428	1.2–15.9	1.25	2.25	2.0–344	0.09–120000	1–1380	1.6–21.0	0.07–1.7	0.17–4710	2.8–1070	0.11–18.2
1ES 2037+521	1.1–15.6	1.30	2.30	2.0–401	0.002–7810	1–1480	1.6–29.2	0.16–6.6	0.15–6410	0.06–103	0.10–35.3
RGB J2042+244	1.0–15.6	1.50	2.50	2.0–468	0.09–150000	1–1410	1.6–33.5	0.80–38.0	0.16–871	0.06–234	0.11–46.5
1ES 0229+200	1.1–13.7	1.10	2.10	2.8–468	0.004–11130	1–1360	1.9–33.2	0.004–0.14	0.31–8710	0.11–140	0.15–45.6

Notes. Columns from left to right: minimum electron Lorentz factor, spectral index of the electron/proton energy distribution below and above $\gamma_{\rm break}$, magnetic field, normalization of the electron distribution, radius of the emission zone, maximum proton Lorentz factor, efficiency of the acceleration mechanism, magnetic energy density, ratio between the proton and magnetic energy densities, and luminosity of the emission region.
[a] These quantities are derived quantities and not model parameters.
[b] The luminosity of the emitting region has been calculated as $L = 2\pi R^2 c \Gamma^2_{\rm bulk}(u_B + u_e + u_p)$, where $\Gamma_{\rm bulk} = \delta/2$, and u_B, u_e, and u_p, the energy densities of the magnetic field, the electrons, and the protons, respectively.

Appendix F
RBS 0921: SED

Figure 10 shows the broadband SED of RBS 0921. Due to the lack of gamma-ray spectral data both in the HE and VHE bands, the SED of this source was not considered for modeling.

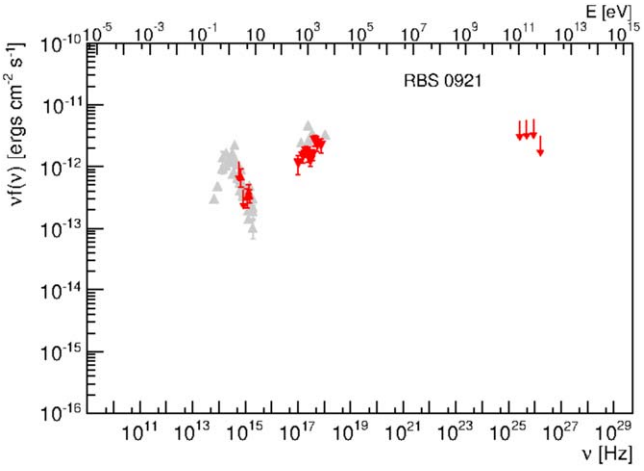

Figure 10. SED of RBS 0921. The unique source of the sample is still undetected at gamma-rays.
(The data used to create this figure are available.)

Appendix G
Maximum Neutrino Flux Expectations

In Figure 11, the maximum neutrino flux expected from the proton synchrotron model for the six sources considered is reported.

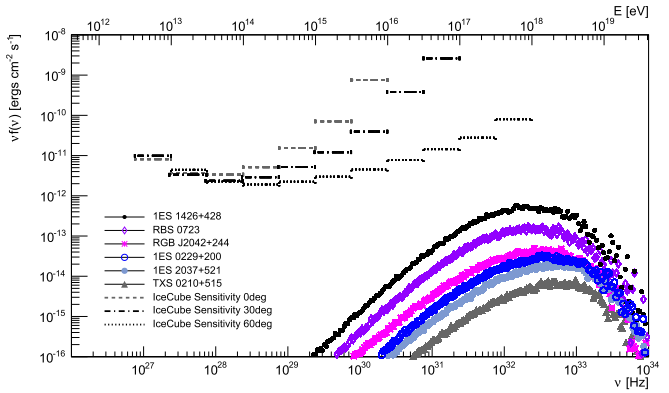

Figure 11. The maximum neutrino flux expected from the proton synchrotron model applied to six EHBLs. The IceCube sensitivity (IceCube Collaboration et al. 2019) for three different declinations is also represented.

ORCID iDs

V. A. Acciari https://orcid.org/0000-0001-8307-2007
S. Ansoldi https://orcid.org/0000-0002-5613-7693
L. A. Antonelli https://orcid.org/0000-0002-5037-9034
K. Asano https://orcid.org/0000-0001-9064-160X
A. Babić https://orcid.org/0000-0002-1444-5604
B. Banerjee https://orcid.org/0000-0002-8008-2485
U. Barres de Almeida https://orcid.org/0000-0001-7909-588X
J. A. Barrio https://orcid.org/0000-0002-0965-0259
J. Becerra González https://orcid.org/0000-0002-6729-9022
W. Bednarek https://orcid.org/0000-0003-0605-108X
E. Bernardini https://orcid.org/0000-0003-3108-1141
A. Berti https://orcid.org/0000-0003-0396-4190
W. Bhattacharyya https://orcid.org/0000-0003-4751-0414
C. Bigongiari https://orcid.org/0000-0003-3293-8522

A. Biland https://orcid.org/0000-0002-1288-833X
O. Blanch https://orcid.org/0000-0002-8380-1633
G. Bonnoli https://orcid.org/0000-0003-2464-9077
Ž. Bošnjak https://orcid.org/0000-0002-6551-4913
G. Busetto https://orcid.org/0000-0002-2687-6380
R. Carosi https://orcid.org/0000-0002-4137-4370
M. Cerruti https://orcid.org/0000-0001-7891-699X
Y. Chai https://orcid.org/0000-0003-2816-2821
A. Chilingaryan https://orcid.org/0000-0002-2018-9715
S. M. Colak https://orcid.org/0000-0001-7793-3106
E. Colombo https://orcid.org/0000-0002-3700-3745
J. L. Contreras https://orcid.org/0000-0001-7282-2394
J. Cortina https://orcid.org/0000-0003-4576-0452
S. Covino https://orcid.org/0000-0001-9078-5507
V. D'Elia https://orcid.org/0000-0002-7320-5862
F. Dazzi https://orcid.org/0000-0001-5409-6544
A. De Angelis https://orcid.org/0000-0002-3288-2517
B. De Lotto https://orcid.org/0000-0003-3624-4480
M. Delfino https://orcid.org/0000-0002-9468-4751
J. Delgado https://orcid.org/0000-0002-0166-5464
D. Depaoli https://orcid.org/0000-0002-2672-4141
F. Di Pierro https://orcid.org/0000-0003-4861-432X
L. Di Venere https://orcid.org/0000-0003-0703-824X
E. Do Souto Espiñeira https://orcid.org/0000-0001-6974-2676
D. Dominis Prester https://orcid.org/0000-0002-9880-5039
A. Donini https://orcid.org/0000-0002-3066-724X
M. Doro https://orcid.org/0000-0001-9104-3214
D. Elsaesser https://orcid.org/0000-0001-6796-3205
V. Fallah Ramazani https://orcid.org/0000-0001-8991-7744
G. Ferrara https://orcid.org/0000-0002-1137-6252
D. Fidalgo https://orcid.org/0000-0002-7480-2730
L. Foffano https://orcid.org/0000-0002-0709-9707
M. V. Fonseca https://orcid.org/0000-0003-2235-0725
L. Font https://orcid.org/0000-0003-2109-5961
C. Fruck https://orcid.org/0000-0001-5880-7518
R. J. García López https://orcid.org/0000-0002-8204-6832
M. Garczarczyk https://orcid.org/0000-0002-0445-4566
M. Gaug https://orcid.org/0000-0001-8442-7877
N. Giglietto https://orcid.org/0000-0002-9021-2888
F. Giordano https://orcid.org/0000-0002-8651-2394
N. Godinović https://orcid.org/0000-0002-4674-9450
D. Green https://orcid.org/0000-0003-0768-2203
D. Guberman https://orcid.org/0000-0002-9636-1825
D. Hadasch https://orcid.org/0000-0001-8663-6461
A. Hahn https://orcid.org/0000-0003-0827-5642
J. Herrera https://orcid.org/0000-0002-3771-4918
J. Hoang https://orcid.org/0000-0001-5591-5927
D. Hrupec https://orcid.org/0000-0002-7027-5021
M. Hütten https://orcid.org/0000-0002-2133-5251
S. Inoue https://orcid.org/0000-0003-1096-9424
D. Kerszberg https://orcid.org/0000-0002-5289-1509
H. Kubo https://orcid.org/0000-0001-9159-9853
A. Lamastra https://orcid.org/0000-0003-2403-913X
D. Lelas https://orcid.org/0000-0002-8269-5760
F. Leone https://orcid.org/0000-0001-7626-3788
E. Lindfors https://orcid.org/0000-0002-9155-6199
S. Lombardi https://orcid.org/0000-0002-6336-865X
F. Longo https://orcid.org/0000-0003-2501-2270
M. López https://orcid.org/0000-0002-8791-7908
R. López-Coto https://orcid.org/0000-0002-3882-9477
A. López-Oramas https://orcid.org/0000-0003-4603-1884
S. Loporchio https://orcid.org/0000-0003-4457-5431
B. Machado de Oliveira Fraga https://orcid.org/0000-0002-6395-3410
C. Maggio https://orcid.org/0000-0003-0670-7771
P. Majumdar https://orcid.org/0000-0002-5481-5040
M. Makariev https://orcid.org/0000-0002-1622-3116
M. Mallamaci https://orcid.org/0000-0003-4068-0496
G. Maneva https://orcid.org/0000-0002-5959-4179
M. Manganaro https://orcid.org/0000-0003-1530-3031
M. Mariotti https://orcid.org/0000-0003-3297-4128
M. Martínez https://orcid.org/0000-0002-9763-9155
D. Mazin https://orcid.org/0000-0002-2010-4005
S. Mićanović https://orcid.org/0000-0002-0076-3134
D. Miceli https://orcid.org/0000-0002-2686-0098
J. M. Miranda https://orcid.org/0000-0002-1472-9690
E. Molina https://orcid.org/0000-0003-1204-5516
A. Moralejo https://orcid.org/0000-0002-1344-9080
D. Morcuende https://orcid.org/0000-0001-9400-0922
V. Moreno https://orcid.org/0000-0002-8358-2098
E. Moretti https://orcid.org/0000-0001-5477-9097
P. Munar-Adrover https://orcid.org/0000-0002-1942-7376
V. Neustroev https://orcid.org/0000-0003-4772-595X
C. Nigro https://orcid.org/0000-0001-8375-1907
K. Nilsson https://orcid.org/0000-0002-1445-8683
D. Ninci https://orcid.org/0000-0002-5031-1849
K. Nishijima https://orcid.org/0000-0002-1830-4251
K. Noda https://orcid.org/0000-0003-1397-6478
L. Nogués https://orcid.org/0000-0002-6482-1671
S. Paiano https://orcid.org/0000-0002-2239-3373
M. Palatiello https://orcid.org/0000-0002-4124-5747
D. Paneque https://orcid.org/0000-0002-2830-0502
R. Paoletti https://orcid.org/0000-0003-0158-2826
J. M. Paredes https://orcid.org/0000-0002-1566-9044
M. Peresano https://orcid.org/0000-0002-7537-7334
M. Persic https://orcid.org/0000-0003-1853-4900
P. G. Prada Moroni https://orcid.org/0000-0001-9712-9916
E. Prandini https://orcid.org/0000-0003-4502-9053
I. Puljak https://orcid.org/0000-0001-7387-3812
W. Rhode https://orcid.org/0000-0003-2636-5000
M. Ribó https://orcid.org/0000-0002-9931-4557
J. Rico https://orcid.org/0000-0003-4137-1134
C. Righi https://orcid.org/0000-0002-1218-9555
A. Rugliancich https://orcid.org/0000-0001-5471-4701
L. Saha https://orcid.org/0000-0002-3171-5039
N. Sahakyan https://orcid.org/0000-0003-2011-2731
K. Satalecka https://orcid.org/0000-0002-7669-266X
K. Schmidt https://orcid.org/0000-0002-3418-7251
J. Sitarek https://orcid.org/0000-0002-1659-5374
A. Somero https://orcid.org/0000-0001-6566-9192
A. Stamerra https://orcid.org/0000-0002-9430-5264
D. Strom https://orcid.org/0000-0003-2108-3311
Y. Suda https://orcid.org/0000-0002-2692-5891
M. Takahashi https://orcid.org/0000-0002-0574-6018
F. Tavecchio https://orcid.org/0000-0003-0256-0995
P. Temnikov https://orcid.org/0000-0002-9559-3384
T. Terzić https://orcid.org/0000-0002-4209-3407
N. Torres-Albà https://orcid.org/0000-0003-3638-8943
V. Vagelli https://orcid.org/0000-0002-4495-9331
J. van Scherpenberg https://orcid.org/0000-0002-6173-867X
M. Vazquez Acosta https://orcid.org/0000-0002-2409-9792
C. F. Vigorito https://orcid.org/0000-0002-0069-9195

V. Vitale https://orcid.org/0000-0001-8040-7852
I. Vovk https://orcid.org/0000-0003-3444-3830
M. Will https://orcid.org/0000-0002-7504-2083
D. Zarić https://orcid.org/0000-0001-5763-9487
C. Arcaro https://orcid.org/0000-0002-1998-9707
A. Carosi https://orcid.org/0000-0001-8690-6804
F. D'Ammando https://orcid.org/0000-0001-7618-7527

References

Abdo, A. A., Ackermann, M., Agudo, I., et al. 2010a, ApJ, 716, 30
Abdo, A. A., Ackermann, M., Ajello, M., et al. 2010b, ApJ, 708, 1310
Abdo, A. A., Ackermann, M., Ajello, M., et al. 2011, ApJ, 736, 131
Acero, F., Ackermann, M., Ajello, M., et al. 2015, ApJS, 218, 23
Ackermann, M., Ajello, M., Allafort, A., et al. 2013, ApJS, 209, 34
Ackermann, M., Ajello, M., Atwood, W. B., et al. 2016, ApJS, 222, 5
Aharonian, F., Akhperjanian, A., Barrio, J., et al. 2002, A&A, 384, L23
Aharonian, F., Akhperjanian, A., Beilicke, M., et al. 2003, A&A, 403, 523
Aharonian, F., Akhperjanian, A. G., Barres de Almeida, U., et al. 2007, A&A, 475, L9
Ahn, C. P., Alexandroff, R., Allende Prieto, C., et al. 2012, ApJS, 203, 21
Ajello, M., Atwood, W. B., Baldini, L., et al. 2017, ApJS, 232, 18
Aleksić, J., Ansoldi, S., Antonelli, L. A., et al. 2016a, APh, 72, 61
Aleksić, J., Ansoldi, S., Antonelli, L. A., et al. 2016b, APh, 72, 76
Aliu, E., Archambault, S., Arlen, T., et al. 2014, ApJ, 782, 13
Archambault, S., Archer, A., Benbow, W., et al. 2016, AJ, 151, 142
Archambault, S., Archer, A., Benbow, W., et al. 2017, ApJ, 835, 288
Asano, K., & Hayashida, M. 2015, ApJL, 808, L18
Asano, K., & Hayashida, M. 2018, ApJ, 861, 31
Asano, K., Takahara, F., Kusunose, M., Toma, K., & Kakuwa, J. 2014, ApJ, 780, 64
Atwood, W. B., Abdo, A. A., Ackermann, M., et al. 2009, ApJ, 697, 1071
Benbow, W. & for the VERITAS Collaboration 2011, ICRC (Beijing), 8, 47
Bonnoli, G., Tavecchio, F., Ghisellini, G., & Sbarrato, T. 2015, MNRAS, 451, 611
Böttcher, M., Reimer, A., Sweeney, K., & Prakash, A. 2013, ApJ, 768, 54
Burrows, D. N., Hill, J. E., Nousek, J. A., et al. 2004, Proc. SPIE, 5165, 201
Burrows, D. N., Hill, J. E., Nousek, J. A., et al. 2005, SSRv, 120, 165
Cerruti, M., Zech, A., Boisson, C., et al. 2019, MNRAS, 483, L12
Cerruti, M., Zech, A., Boisson, C., & Inoue, S. 2015, MNRAS, 448, 910
Chang, Y.-L., Arsioli, B., Giommi, P., & Padovani, P. 2017, A&A, 598, A17
Cooray, A. 2016, RSOS, 3, 150555
Costamante, L., Bonnoli, G., Tavecchio, F., et al. 2018, MNRAS, 477, 4257
Costamante, L., Ghisellini, G., Giommi, P., et al. 2001, A&A, 371, 512
de la Calle Pérez, I., Bond, I. H., Boyle, P. J., et al. 2003, ApJ, 599, 909
Djannati-Ataï, A., Khelifi, B., Vorobiov, S., et al. 2002, A&A, 391, L25
Domínguez, A., Primack, J. R., Rosario, D. J., et al. 2011, MNRAS, 410, 2556
Evans, P. A., Beardmore, A. P., Page, K. L., et al. 2009, MNRAS, 397, 1177
Fallah Ramazani, V., Lindfors, E., & Nilsson, K. 2017, A&A, 608, A68
Fidelis, V. 2012, Ap, 55, 226
Foffano, L., Prandini, E., Franceschini, A., & Paiano, S. 2019, MNRAS, 486, 1741
Fossati, G., Maraschi, L., Celotti, A., Comastri, A., & Ghisellini, G. 1998, MNRAS, 299, 433
Franceschini, A., Rodighiero, G., & Vaccari, M. 2008, A&A, 487, 837
Gao, S., Fedynitch, A., Winter, W., & Pohl, M. 2018, NatAs, 3, 88
Ghisellini, G. 1999, APh, 11, 11
Ghisellini, G., & Celotti, A. 2001, MNRAS, 327, 739
Ghisellini, G., Celotti, A., Fossati, G., Maraschi, L., & Comastri, A. 1998, MNRAS, 301, 451
Ghisellini, G., Maraschi, L., & Tavecchio, F. 2009, MNRAS, 396, L105
Ghisellini, G., Righi, C., Costamante, L., & Tavecchio, F. 2017, MNRAS, 469, 255
Ghisellini, G., Tavecchio, F., & Chiaberge, M. 2005, A&A, 432, 401
Giommi, P., Padovani, P., Polenta, G., et al. 2011, MNRAS, 420, 2899
Harrison, F. A., Craig, W. W., Christensen, F. E., et al. 2013, ApJ, 770, 103
Hayashida, M., Madejski, G. M., Nalewajko, K., et al. 2012, ApJ, 754, 114
Horan, D., Badran, H. M., Bond, I. H., et al. 2002, ApJ, 571, 753
IceCube Collaboration, Aartsen, M. G., Ackermann, M., et al. 2018, Sci, 361, eaat1378
IceCube Collaboration, Aartsen, M. G., Ackermann, M., et al. 2019, EPJC, 79, 234
Kalberla, P. M. W., Burton, W. B., Hartmann, D., et al. 2005, A&A, 440, 775
Kataoka, J., Madejski, G., Sikora, M., et al. 2008, ApJ, 672, 787
Kaufmann, S., Wagner, S. J., Tibolla, O., & Hauser, M. 2011a, A&A, 534, A130
Kaufmann, S., Wagner, S. J., Tibolla, O., & Hauser, M. 2011b, A&A, 534, A130
Kaur, A., Rau, A., Ajello, M., et al. 2018, ApJ, 859, 80
Keivani, A., Murase, K., Petropoulou, M., et al. 2018, ApJ, 864, 84
Kino, M., Takahara, F., Hada, K., et al. 2015, ApJ, 803, 30
Komissarov, S. S., Vlahakis, N., Königl, A., & Barkov, M. V. 2009, MNRAS, 394, 1182
Li, T.-P., & Ma, Y.-Q. 1983, ApJ, 272, 317
Madsen, K. K., Beardmore, A. P., Forster, K., et al. 2017, AJ, 153, 2
MAGIC Collaboration, Acciari, V. A., Ansoldi, S., et al. 2019a, MNRAS, 490, 2284
MAGIC Collaboration, Acciari, V. A., Ansoldi, S., et al. 2019b, MNRAS, 486, 4233
MAGIC Collaboration, Ahnen, M. L., Ansoldi, S., et al. 2017a, MNRAS, 468, 1534
MAGIC Collaboration, Ahnen, M. L., Ansoldi, S., et al. 2017b, APh, 94, 29
MAGIC Collaboration, Ahnen, M. L., Ansoldi, S., et al. 2018, A&A, 620, A181
Mao, L. S. 2011, NewA, 16, 503
Maraschi, L., & Tavecchio, F. 2003, ApJ, 593, 667
Massaro, E., Perri, M., Giommi, P., & Nesci, R. 2004, A&A, 413, 489
Moderski, R., Sikora, M., & Błażejowski, M. 2003, A&A, 406, 855
Moralejo, A., Gaug, M., Carmona, E., et al. 2009, arXiv:0907.0943
Murase, K., Dermer, C. D., Takami, H., & Migliori, G. 2012, ApJ, 749, 63
Nakamura, M., & Asada, K. 2013, ApJ, 775, 118
Oh, K., Koss, M., Markwardt, C. B., et al. 2018, ApJS, 235, 4
Padovani, P. 2007, Ap&SS, 309, 63
Padovani, P. 2016, A&ARv, 24, 13
Padovani, P., Alexander, D. M., Assef, R. J., et al. 2017, A&ARv, 25, 2
Petry, D., Bond, I. H., Bradbury, S. M., et al. 2002, ApJ, 580, 104
Pian, E., Vacanti, G., Tagliaferri, G., et al. 1998, ApJL, 492, L17
Sanchez, D. A., & Deil, C. 2014, Braz. J. Phys., 44, 415
Shaw, M. S., Romani, R. W., Cotter, G., et al. 2013, ApJ, 764, 135
Sironi, L., Petropoulou, M., & Giannios, D. 2015, MNRAS, 450, 183
Sironi, L., & Spitkovsky, A. 2014, ApJL, 783, L21
Sowards-Emmerd, D., Romani, R. W., Michelson, P. F., Healey, S. E., & Nolan, P. L. 2005, ApJ, 626, 95
Stickel, M., Padovani, P., Urry, C. M., Fried, J. W., & Kuehr, H. 1991, ApJ, 374, 431
Stocke, J. T., Morris, S. L., Gioia, I. M., et al. 1991, ApJS, 76, 813
Stroh, M. C., & Falcone, A. D. 2013, ApJS, 207, 28
Tavecchio, F., & Ghisellini, G. 2008, MNRAS, 385, L98
Tavecchio, F., & Ghisellini, G. 2015, MNRAS, 456, 2374
Tavecchio, F., Ghisellini, G., Ghirlanda, G., Costamante, L., & Franceschini, A. 2009, MNRAS, 399, L59
Tavecchio, F., Ghisellini, G., Ghirlanda, G., Foschini, L., & Maraschi, L. 2010, MNRAS, 401, 1570
Urry, C. M., & Padovani, P. 1995, PASP, 107, 803
Vovk, I., Taylor, A. M., Semikoz, D., & Neronov, A. 2012, ApJL, 747, L14
Willingale, R., Starling, R. L. C., Beardmore, A. P., Tanvir, N. R., & O'Brien, P. T. 2013, MNRAS, 431, 394
Zanin, R. 2013, ICRC (Rio de Janeiro), 44, 415
Zdziarski, A. A., & Böttcher, M. 2015, MNRAS, 450, L21